A&A 518, A9 (2010)
DOI: 10.1051/0004-6361/200913392


Astronomy & Astrophysics

# TANGO I: Interstellar medium in nearby radio galaxies

## Molecular gas⋆

B. Ocaña Flaquer[1], S. Leon[2,1], F. Combes[3], and J. Lim[4,5]

[1] Instituto de Radio Astronomía Milimétrica (IRAM), Av. Divina Pastora, 7, Núcleo Central, 18012 Granada, Spain
e-mail: ocana@iram.es
[2] Joint Alma Observatory/ESO, Av. El Golf 40, Piso 18, Las Condes, Santiago, Chile
e-mail: sleon@alma.cl
[3] Observatoire de Paris, LERMA, 61 Av. de l'Observatoire, 75014 Paris, France
e-mail: francoise.combes@obspm.fr
[4] Institute of Astronomy and Astrophysics, Academia Sinica,128, Sect. 2, Yen Geo Yuan Road, Nankang, Taipei, Taiwan, R.O.C.
e-mail: lim@asiaa.sinica.edu.tw
[5] Department of Physics, University of Hong Kong, Pokfulam Road, Hong Kong
e-mail: jjlim@hku.hk

Received 1 October 2009 / Accepted 26 January 2010

**ABSTRACT**

*Context.* Powerful radio-AGN are hosted by massive elliptical galaxies that are usually very poor in molecular gas. Nevertheless, gas is needed at their very center to feed the nuclear activity.
*Aims.* We study the molecular gas properties (i.e., mass, kinematics, distribution, origin) of these objects, and compare them with results for other known samples.
*Methods.* At the IRAM-30m telescope, we performed a survey of the CO(1-0) and CO(2-1) emission from the most powerful radio galaxies of the Local Universe, selected only on the basis of their radio continuum fluxes.
*Results.* The main result of our survey is that the molecular gas content of these galaxies is very low compared to spiral or FIR-selected galaxies. The median value of the molecular gas mass, including detections and upper limits, is $2.2 \times 10^8\ M_\odot$. When separated into FR-I and FR-II types, a difference in their $H_2$ masses is found. The median value of FR-I galaxies is about $1.9 \times 10^8\ M_\odot$ and higher for FR-II galaxies, at about $4.5 \times 10^8\ M_\odot$. Which is probably entirely because of a Malmquist bias. Our results contrast with those of previous surveys, whose targets were mainly selected by means of their FIR emission, implying that we measure higher observed masses of molecular gas. Moreover, the shape of CO spectra suggest that a central molecular gas disk exists in 30% of these radio galaxies, a lower rate than in other active galaxy samples.
*Conclusions.* We find a low level of molecular gas in our sample of radio-selected AGNs, indicating that galaxies do not need much molecular gas to host an AGN. The presence of a molecular gas disk in some galaxies and the wide range of molecular gas masses may be indicative of different origins for the gas, which we can not exclude at present (e.g., minor/major mergers, stellar mass loss, or accretion).

**Key words.** Galaxy: evolution – galaxies: luminosity function, mass function – radio continuum: galaxies

## 1. Introduction

Radio galaxies contain strong radio sources with power in the range of $10^{41}$ to $10^{46}$ erg/s, equivalent to $10^{34}$–$10^{39}$ Watts, normally hosted by giant elliptical galaxies with visual luminosities of about $2.1 \times 10^{10}\ h^{-2}\ L_\odot$ (Kellermann & Verschuur (1988), calculated with a Hubble constant of $H = 100\ \mathrm{km\,s^{-1}\,Mpc^{-1}}$). Although in general quite deficient in cold gas, elliptical galaxies do contain some dense and cold interstellar medium (ISM) detected in CO(1-0) emission (e.g., Wiklind & Rydbeck 1986). Dust is also detected in the far-infrared (FIR) radiation which is assumed to be thermal and to originate in dust heated by young massive stars or active galactic nuclei (AGN) (Knapp et al. 1989; Wiklind & Henkel 1995). According to Kennicutt (1998), early-type galaxies show no independent evidence of high star-formation rates (SFRs), suggesting that the older stars or the AGN are responsible for much of the FIR emission.

In elliptical galaxies, Wiklind & Henkel (1995) show that the gas is unrelated to the stellar populations, and favor an external origin of the molecular gas. It is widely believed that the AGN are powered by accretion of ISM onto supermassive black holes (SMBHs) (Antonucci 1993). According to de Ruiter et al. (2002), an ISM in the circumnuclear regions of AGN should be present and the large-scale dust/gas systems should be related to nuclear activity. Hardcastle et al. (2007) propose that all the apparently different accretion modes may be the result of a different source for the accreting gas. This hypothesis was considered earlier by Allen et al. (2006), who demonstrated that some low luminosity radio galaxies in the center of clusters could be powered by Bondi accretion, a spherical accretion of the hot, X-ray emitting medium. The accretion mode of low power radio sources was also discussed by Best et al. (2006).

⋆ Appendices and Figure 15 are only available in electronic form at http://www.aanda.org

For low-luminosity AGN, the stellar component might provide sufficient fuel for the active nucleus, but in powerful radio galaxies large-scale dynamical processes are required to transfer the angular momentum of the interstellar gas across the disk radius (Shlosman et al. 1990; Combes 2002). Fueling also depends on the morphological type of the galaxy, since the radial gas flows are driven by non-axisymmetric instabilities, and the stability of the disk depends on the bulge-to-disk ratio (Mihos & Hernquist 1996, 1994). In early-type galaxies, for example, once the accreted gas has settled in to a symmetric disk, the large-mass black holes (BH) begin to starve, unless the gas is perturbed by an external tide (e.g., Combes 2002). To understand the role of the ISM in radio galaxies more clearly, we compiled two samples, at low and medium redshift, of radio galaxies selected only on the basis of their radio continuum emission.

This is the first paper of the Thorough ANalysis of radio-Galaxies Observation (TANGO) project in a series that will cover a wide range of wavelengths (optical, radio, IR, X-ray). An observational criterion for inclusion in the TANGO samples at low and medium redshift is that most of the objects are visible from the main (radio) telescopes of the northern and southern hemispheres, such as ALMA, IRAM telescopes, VLA, VLT, GTC among others. We study primarily the molecular gas by means of the CO emission in the low-redshift TANGO sample of radio galaxies ($z \leq 0.1$). We test, in particular, whether samples selected on the basis of their FIR emission, e.g., Evans et al. (2005), and radio continuum-selected samples behave in similar ways.

This paper is structured as follows: we describe the sample of radio galaxies, their observations, and their data reduction process in Sect. 2. The molecular gas properties are described in Sect. 3, while the dust properties are described in Sect. 4 and the gas and dust relations are discussed in Sect. 5. Section 6 is dedicated to the comparison of our results with those of similar samples. Finally, our discussion and conclusions are drawn in Sects. 7 and 8, respectively. Properties of individual galaxies are presented in Appendix A, the beam/source coupling is explained in detail in Appendices B, and C is dedicated to the detailed analysis of one of the galaxies in TANGO, 3CR 31.

## 2. Observation and data reduction

### 2.1. Sample

As mentioned in the introduction, galaxies selected for the low and medium redshift TANGO sample have one main criterion of selection: a high radio continuum power. Thus, in the low redshift sample studied in this paper, all radio galaxies have a radio power at 1.4 GHz greater than $10^{22.5}$ W Hz$^{-1}$ with a median of $10^{24.4}$ W Hz$^{-1}$. This represents the main difference with previous samples chosen e.g., on the basis of their FIR flux (e.g., Evans et al. 2005).

This work studies a total of 52 nearby radio galaxies, most of them from the Third Cambridge Catalog (3CR – Edge et al. 1959; Bennett 1962), New General Catalog (NGC – Dreyer 1888), and the Second Bologna Catalog of Radio Sources (B2 – Colla et al. 1970, 1972, 1973; Fanti et al. 1974). There is one galaxy from the Ohio State University Radio survey Catalog (OQ – Scheer & Kraus 1967) and one galaxy from the Uppsala General Catalogue of Galaxies (UGC – Nilson 1973). The details of the catalogs for the sample are summarized in Table 1.

**Table 1.** The catalogs are listed in order of importance, some galaxies are in more than one catalog with different names.

| Catalog name | # of galaxies | % of detection [1] |
|---|---|---|
| 3CR | 24 | 58% |
| NGC | 13 | 62% |
| B2 | 13 | 31% |
| UGC | 1 | 0.0% |
| OQ | 1 | 100.0% |
| **Total** | 52 | 52% |

**Notes.** In this article, the names are chosen first in favor of the 3CR catalog and last for the OQ catalog. [(1)] This % is within the catalog, meaning the percentage of galaxies detected in each catalog.

### 2.2. Observations

This work is based on a survey of the $^{12}$CO(1-0) and $^{12}$CO(2-1) transitions, simultaneously observed with the IRAM 30 m telescope, at Pico Veleta, Spain, reaching an rms temperature of about 0.6 mK with a velocity resolution between 20 km s$^{-1}$ and 52 km s$^{-1}$. The transitions were observed at 115.27 GHz and 230.54 GHz (where the beam of the IRAM-30m telescope is about 22 and 11 arcsec), redshifted to the velocity of the galaxies, for $^{12}$CO(1-0) and $^{12}$CO(2-1) with the A and B receivers, respectively. The filter backends were configured into two units of $512 \times 1$ MHz channels and two units of $512 \times 4$ MHz, one for each receiver. During the observations, the pointing and focus were monitored by observing planets and standard continuum sources every hour with an accuracy of about 3″.

From the total of 52 galaxies in the sample, all were observed in the CO(1-0) line and 43 galaxies were simultaneously observed in CO(2-1) line, when the weather permitted. About 58% of galaxies ($N = 30$) in the sample were detected (clearly or tentatively) in one or both lines, and 38% of the galaxies ($N = 20$) were clearly detected, some of them only in CO(1-0), some only in CO(2-1) and some in both CO transitions. A total of 7 galaxies were detected in both lines, these galaxies being 3CR 31, 3CR 264, NGC 326, NGC 4278, NGC 7052, B2 0116+31, and B2 0648+27. These 7 galaxies were used to study the CO(2-1)-to-CO(1-0) line ratios discussed in Sect. 3.2 in more detail. There were 9 galaxies for which we only have data in the 3 mm wavelength range (3CR 236, 3CR 305, 3CR 321, 3CR 327, 3CR 403, 3CR 433, NGC 6251, B2 0836+29, and OQ 208), where 6 of them show a clear detection (3CR 305, 3CR 321, 3CR 327, 3CR 403, B2 0836+29, and OQ208). Table 2 is a journal of the observations that shows the dates on which each detected galaxy was observed.

This project started in 1999 and the last observations are from the year 2007, some of the galaxies were observed several times throughout this 8 year period to confirm some possible detections. Part of this work was published by Lim et al. (2000) in a detailed study of the galaxies 3C31 and 3C264.

We also observed the CO(1-0) emission at the center of 3C31 using the IRAM Plateau de Bure Interferometer (PdBI). We used several tracks in the B configuration. The velocity resolution was set to be 20 km s and the CLEANed maps were restored with a synthesized beam of $2\farcs2 \times 1\farcs2$ (PA=47°). See Appendix C for an example of this analysis.

### 2.3. Data reduction

To perform the data reduction, the Continuum and Line Analysis Single-dish Software (CLASS) was used. All spectra were

**Table 2.** Journal observations for the 30 detected galaxies in the sample.

| **Galaxy** | Observation dates | **Galaxy** | Observation dates |
|---|---|---|---|
| 3*C*31 | 1999 Dec. | *NGC* 315 | 2002 Jun. |
| | 2000 Jan. | | 2006 Oct. |
| 3*C*66*BB* | 2000 Jan. | | 2007 Apr. |
| | 2003 May | *NGC* 326 | 2006 Oct. |
| 3*C*83.1 | 2000 Jan. | *NGC* 541 | 2002 Jun. |
| 3*C*88 | 1999 Dec. | *NGC* 708 | 2006 Oct. |
| | 2000 Jan. | *NGC* 3801 | 2002 Jun |
| 3*C*129 | 2000 Jan. | *NGC* 4278 | 2007 Jan. |
| 3*C*264 | 2000 Jan. | | 2007 Apr. |
| 3*C*272.1 | 2000 Jan. | *NGC* 5127 | 2002 Jun. |
| 3*C*274 | 2000 Jan. | *NGC* 7052 | 2002 Jun. |
| 3*C*305 | 2004 Feb. | | 2006 Jul. |
| | 2004 Mar. | *B*2 0116 + 31 | 2003 Dec. |
| 3*C*321 | 2004 Mar. | | 2006 Jun. |
| 3*C*327 | 2004 Mar. | | 2006 Oct. |
| 3*C*353 | 2000 Jan. | *B*2 0648 + 27 | 2004 Feb. |
| 3*C*386 | 1999 Dec. | | 2004 Mar. |
| 3*C*403 | 2003 Dec. | | 2006 Oct. |
| | 2004 Feb. | *B*2 0836 + 29*B* | 2004 Mar. |
| 3*C*442 | 2000 Jan. | *B*2 0924 + 30 | 2007 Apr. |
| 3*C*449 | 1999 Dec. | *B*2 1347 + 28 | 2007 Jan. |
| | 2000 Jan. | | 2007 Apr. |
| | | *OQ*208 | 2004 Mar. |

individually checked, those of poor quality were removed, and the remaining spectra of the same frequency were added. The baseline was removed after selecting a window. This window was taken to be the velocity width for the detected galaxies, and a line-width value of ∼300 km s$^{-1}$ was applied to compute the upper limits. Each spectra was smoothed to a velocity resolution of between 20 and 50 km s$^{-1}$. The integrated intensity, velocity width, position and peak temperature of the galaxies were determined by fitting a Gaussian. The result spectra of each detected galaxy can be found in the online material, Table 1.

We use the baseline of the spectra to calculate the continuum flux at 3 and 1 mm. The continuum level and the detections were given in antenna temperature, $T_a^*$, and then converted to a main beam temperature, $T_{\rm MB}$. The conversion factor used was that one given by Rohlfs & Wilson (2004), where we divided the forward efficiency, which is a model function to the measure antenna temperature and the copper load temperature, by the beam efficiency, which is the percentage of all power received that enters the main beam, $F_{\rm eff}/B_{\rm eff}$. Applying this to each frequency for the IRAM-30m telescope, the relationship is 1.27 at 3 mm and 1.75 at 1 mm.

To convert the data from temperature (K) to flux (Jy), the point-source sensitivity measurement ($S/T_A^*$) is 6.3 for 3 mm and 8 for 1 mm wavelength. The results for these conversions are listed in Table 3. For more details of the conversion, we refere to Kramer (1997). From the observations, to summarize, 90% of the 52 galaxies were detected in the continuum at 3 mm and 65% out of the 43 galaxies were detected in the continuum at 1 mm.

**Table 3.** IRAM 30m fluxes at 3 mm and 1 mm.

| **Galaxy** | $S_{3\ \rm mm}$ (mJy) | $\delta S_{3\ \rm mm}$ (mJy) | $S_{1\ \rm mm}$ (mJy) | $\delta S_{1\ \rm mm}$ (mJy) |
|---|---|---|---|---|
| 3*CR*31 | 79.07 | 1.13 | 74.39 | 2.78 |
| 3*CR*40 | 96.91 | 0.9 | 20.11 | 1.8 |
| 3*CR*66*B* | 110.12 | 0.43 | 73.08 | 1.39 |
| 3*CR*83.1 | 33.45 | 0.69 | ... | ... |
| 3*CR*88 | 121.84 | 0.43 | 87.05 | 1.3 |
| 3*CR*98 | 18.09 | 0.52 | 6.18 | 1.54 |
| 3*CR*129 | 28.53 | 0.65 | 0.91 | 1.27 |
| 3*CR*236 | 225.06 | 0.57 | X | X |
| 3*CR*264 | 174.64 | 0.5 | 87.35 | 1.13 |
| 3*CR*270 | 326.34 | 0.82 | 204.71 | 1.57 |
| 3*CR*272.1 | 138.29 | 1.2 | 73.86 | 6.79 |
| 3*CR*274 | 2347.13 | 1.83 | 1312.31 | 2.78 |
| 3*CR*296 | 99.23 | 0.6 | 54.55 | 1.22 |
| 3*CR*305 | 21.23 | 4.28 | X | X |
| 3*CR*321 | 67.33 | 0.52 | X | X |
| 3*CR*327 | 105.81 | 0.69 | X | X |
| 3*CR*353 | ... | ... | 3.46 | 1.35 |
| 3*CR*386 | 50.21 | 0.88 | 105.01 | 2.26 |
| 3*CR*402 | 332.57 | 39.27 | ... | ... |
| 3*CR*403 | 20.35 | 0.48 | X | X |
| 3*CR*433 | 91.29 | 0.76 | X | X |
| 3*CR*442 | 9.62 | 0.43 | 75.51 | 9.99 |
| 3*CR*449 | 25.82 | 0.5 | 15.83 | 1.65 |
| 3*CR*465 | 86.06 | 0.56 | 27.32 | 1.31 |
| *NGC*315 | 353.56 | 0.67 | 62.12 | 1.39 |
| *NGC*326 | 63.47 | 0.63 | ... | ... |
| *NGC*541 | 4.73 | 2.02 | 27.23 | 2.60 |
| *NGC*708 | 8.11 | 0.98 | 148.94 | 3.83 |
| *NGC*2484 | 110.63 | 0.69 | 11.92 | 1.65 |
| *NGC*2892 | 190.05 | 0.87 | 272.39 | 2.23 |
| *NGC*3801 | 1181.72 | 210 | ... | ... |
| *NGC*4278 | 215.9 | 1.08 | 194.34 | 1.28 |
| *NGC*5127 | 25.62 | 1.13 | ... | ... |
| *NGC*5141 | 63.50 | 1.01 | ... | ... |
| *NGC*5490 | 27.72 | 1.44 | 88.61 | 5.46 |
| *NGC*6251 | 367.88 | 0.71 | X | X |
| *NGC*7052 | 85.51 | 12.13 | 18.77 | 1.49 |
| *B*2 0034 + 25 | 72.97 | 0.68 | 190.81 | 1.82 |
| *B*2 0116 + 31 | 164.53 | 1.22 | ... | ... |
| *B*2 0648 + 27 | 152.99 | 0.37 | 172.99 | 2.09 |
| *B*2 0836 + 29*B* | ... | ... | X | X |
| *B*2 0915 + 32*B* | 11.39 | 1.29 | 24.41 | 2.17 |
| *B*2 0924 + 30 | 9.44 | 1.13 | ... | ... |
| *B*2 1101 + 38 | 359.89 | 0.97 | 0.165 | 0.002 |
| *B*2 1347 + 28 | 8.96 | 0.51 | ... | ... |
| *B*2 1357 + 28 | ... | ... | ... | ... |
| *B*2 1447 + 27 | 13.94 | 0.53 | 52.41 | 0.81 |
| *B*2 1512 + 30 | ... | ... | ... | ... |
| *B*2 1525 + 29 | 14.48 | 1.07 | 0.13 | 0.003 |
| *B*2 1553 + 24 | 35.28 | 1 | ... | ... |
| *UGC*7115 | 30.57 | 1.03 | ... | ... |
| *OQ*208 | 40.43 | 16.67 | X | X |

**Notes.** X means that there was no data, and "..." refers to undetected flux.

### 2.4. IRAS data

We use the IRAS data to study the dust properties of both the warm component ($\lambda \sim 60\ \mu$m) associated with young star-forming regions and/or an AGN, and the cooler components ($\lambda \geq 100\ \mu$m) associated with more extended dust that is heated by the interstellar radiation field (Kennicutt 1998). We complemented the 30 m data with the IRAS fluxes taken from the Nasa Extra-galactic Database (NED) for the 60 $\mu$m and 100 $\mu$m wavelengths. From this sample, a total of 38 galaxies were detected by IRAS. Eighteen of them are considered to have a clear detection; 15 galaxies have upper limits for both 60 $\mu$m and 100 $\mu$m wavelengths, and 5 galaxies have upper limits only at 100 $\mu$m, being reliably detected at 60 $\mu$m. For that study, we use hereafter the 18 galaxies that were clearly detected at both wavelengths, these galaxies and their fluxes being listed in Table 4.

**Table 4.** IRAS data for the galaxies detected at 60 $\mu$m and at 100 $\mu$m.

| Galaxy name | $f_{60}$ $\mu$m (mJy) | $f_{100}$ $\mu$m (mJy) |
|---|---|---|
| 3CR 31 | 435 ± 65.3 | 1675 ± 251 |
| 3CR 88 | 180 ± 27 | 816 ± 122 |
| 3CR 272.1 | 556 ± 83.4 | 1024 ± 154 |
| 3CR 274 | 546 ± 81.9 | 559 ± 83.9 |
| 3CR 305 | 298 ± 44.7 | 450 ± 67.5 |
| 3CR 321 | 1067 ± 160 | 961 ± 144 |
| 3CR 327 | 670 ± 101 | 371 ± 55.7 |
| 3CR 402 | 257 ± 38.6 | 1052 ± 158 |
| NGC 315 | 368 ± 55.2 | 460 ± 69 |
| NGC 708 | 200 ± 34 | 660 ± 157 |
| NGC 4278 | 580 ± 53 | 1860 ± 60 |
| NGC 6251 | 188 ± 28.2 | 600 ± 90 |
| NGC 7052 | 524 ± 78.6 | 1150 ± 173 |
| B2 0116+31 | 150 ± 22.5 | 524 ± 78.6 |
| B2 0648+27 | 2633 ± 395 | 1529 ± 229 |
| B2 0836+29B | 472 ± 70.8 | 595 ± 89.2 |
| B2 1101+38 | 181 ± 22 | 361 ± 68 |
| OQ 208 | 753 ± 113 | 1029 ± 154 |

## 3. Molecular gas

### 3.1. Molecular gas mass

In Table 5, we present the results of the observations, where $I_{\mathrm{CO(1-0)}}$ and $I_{\mathrm{CO(2-1)}}$ are the integrated intensities ($\int T_{\mathrm{MB}} \mathrm{d}\upsilon$) for the $^{12}$CO(1-0) and $^{12}$CO(2-1) line respectively, $\delta I_{\mathrm{CO(1-0)}}$ and $\delta I_{\mathrm{CO(2-1)}}$ are the standard error $I_{\mathrm{CO(1-0)}}$ and $I_{\mathrm{CO(2-1)}}$ respectively, $V_{\mathrm{width\ CO(1-0)}}$ and $V_{\mathrm{width\ CO(2-1)}}$ are the velocity width of CO(1-0) and CO(2-1) respectively, and $M_{\mathrm{H_2}}$ is the calculated molecular gas mass for each galaxy in the sample.

We follow Gordon et al. (1992) in deriving $H_2$ masses from the $^{12}$CO(1-0) line observations. Our temperature unit is expressed in a $T_{\mathrm{A}}^*$ antenna temperature scale, which is corrected for atmospheric attenuation and rear side-lobes. The radiation temperature $T_{\mathrm{R}}$ of the extragalactic source is then

$$T_{\mathrm{R}} = \frac{4}{\pi}\left(\frac{\lambda}{D}\right)^2 \frac{K}{\eta_{\mathrm{A}}}\frac{T_{\mathrm{A}}}{\Omega_S}, \tag{1}$$

where $\lambda$ is the observed wavelength (2.6 mm), $D$ is the IRAM radio telescope diameter (30 m), $K$ is the correction factor for the coupling of the sources with the beam, $\eta_{\mathrm{A}}$ is the aperture efficiency (0.55) at 115 GHz, $T_{\mathrm{A}}$ is an antenna temperature which is $F_{\mathrm{eff}}T_{\mathrm{A}}^*$ in the IRAM convention explicitly written as $T_{\mathrm{A}} = 0.92T_{\mathrm{A}}^*$, and $\Omega_S$ is the source solid angle.

Without taking into account the cosmological correction, because of the low redshift, and using the standard CO-to-$H_2$ conversion factor $2.3\times10^{20}$ cm$^{-2}$ (K km s$^{-1}$)$^{-1}$ suggested by Strong et al. (1988), the column density of molecular hydrogen can be written as

$$N(\mathrm{H_2}) = 2.3\times10^{20}\int_{\mathrm{line}} T_{\mathrm{R}}\mathrm{d}\upsilon(\mathrm{mol.cm^{-2}}), \tag{2}$$

where d$\upsilon$ is the velocity interval. In Eq. (1), $K \equiv \Omega_{\mathrm{s}}/\Omega_\Sigma$ is the factor that corrects the measured antenna temperature for the weighting of the source distribution by the large antenna beam in the case of a smaller source. We have defined the source solid angle as

$$\Omega_S \equiv \int_{\mathrm{source}} \phi(\theta,\psi)\mathrm{d}\Omega, \tag{3}$$

where $\phi(\theta,\psi)$ is the normalized source brightness distribution function. The beam-weighted source solid angle is

$$\Omega_\Sigma \equiv \int_{\mathrm{source}} \phi(\theta,\psi)f(\theta,\psi)\mathrm{d}\Omega, \tag{4}$$

where $f(\theta,\psi)$ denotes the normalized antenna power pattern (Baars 1973). Experiments have shown that we can approximate $f$ with a Gaussian beam. An exponential law of scale length $h = D_{\mathrm{B}}/10$ is taken to model the source distribution function. The factor 10 is used to estimate the scale length of the molecular gas distribution from the optical diameter ($B$ band). We used our own data from the CO(1-0) map of 3CR 31 and the CO(1-0) map of elliptical galaxies presented by Young (2002). In Eq. (5), the optical diameter is represented by $\theta_{\mathrm{s}}$. By assuming that the gas surface density is given by $\mu(r) \propto \mathrm{e}^{-r/h}$ and that the source is smaller than the beam size, we have the following:

$$K = \frac{\int_0^{\theta_{\mathrm{s}}/2} \sin(\theta) e^{-\frac{10\theta}{\theta_{\mathrm{s}}}}\mathrm{d}\theta}{\int_0^{\theta_{\mathrm{s}}/2} \sin(\theta)\mathrm{e}^{-\frac{10\theta}{\theta_{\mathrm{s}}}-\ln(2)(\frac{2\theta}{\theta_{\mathrm{b}}})^2}\mathrm{d}\theta}\cdot \tag{5}$$

If $I_{\mathrm{CO}}$ is the velocity-integrated temperature for the $^{12}$CO(1-0) line in $T_{\mathrm{A}}^*$ scale given the IRAM-30m parameters, the total mass of $H_2$ is then given by

$$M_{\mathrm{H_2}} = 5.86\times10^4 D^2 K I_{\mathrm{CO}}(M_\odot) \tag{6}$$

at the distance, D, in Mpc.

Using the survival analysis statistics software (ASURV), which takes into account upper limits in addition to detections, we calculated a median value for the molecular gas mass of $2.2\times10^8$ $M_\odot$ (and an average of $3\times10^8$ $M_\odot$) for our complete sample of 52 galaxies. Their molecular gas mass distribution can be seen in Fig. 1. The molecular gas distribution is normalized to one for the whole sample including the detections and the upper limits for CO(1-0) observations. In the same figure we show in darker colors the histogram of only the galaxies detected, the median value of the molecular gas mass of these 30 detected galaxies is then $3.4\times10^8$ $M_\odot$.

To normalize the sample, we divided the distribution per bin of the histogram by the total number of galaxies in the sample, and to normalize the subsample by including the detected galaxies only, we divided the distribution per bin by the total number of galaxies in the complete sample, to be able to compare both samples. The range of the molecular gas mass (in base 10 logarithmic scale) for the sub-group of the detected galaxies is between 6.3 and 10.2. The number of galaxies with a molecular gas mass lower than 6.3 (in log) is obviously unknown.

The molecular gas mass of the sample extends over 4 orders of magnitude, from $3\times10^6$ $M_\odot$ for 3C272.1 to $1.4\times10^{10}$ $M_\odot$ for OQ 208. Most of the galaxies have a molecular gas mass between 8.3 ($2\times10^8$ $M_\odot$) and 8.7 ($5\times10^8$ $M_\odot$), which is also as true for the complete sample including the upper limit calculation as for the subsample that includes only the detected galaxies.

When searching for a relation between the optical luminosity ($L_{\mathrm{B}}$) and the molecular gas mass of the galaxies ($M_{\mathrm{H_2}}$), as shown in Fig. 2, we find that there is no correlation, which is interpreted as implying that the molecular gas mass is independent of the size of the galaxies. The FIR luminosity which is described in more detail in Sect. 5, and the molecular gas mass, normalized by the optical luminosity, also exhibits no correlation, as can be confirmed in Fig. 3.

**Table 5.** Molecular gas data.

| **Galaxy** | $Z_{CO}$ | Distance (Mpc) | $I_{CO(1-0)}$ (K Km s$^{-1}$) | $\delta I_{CO(1-0)}$ (K Km s$^{-1}$) | FWZI$_{CO(1-0)}$ (km s$^{-1}$) | $I_{CO(2-1)}$ (K Km s$^{-1}$) | $\delta I_{CO(2-1)}$ (K Km s$^{-1}$) | FWZI$_{CO(2-1)}$ (km s$^{-1}$) | $M_{H_2}$ ($\times 10^8$ $M_{sun}$) |
|---|---|---|---|---|---|---|---|---|---|
| 3*C*31$^{**,a}$ | 0.0169 | 71.06 | 5.68 | 0.81 | 550 | 14.06 | 1.13 | 550 | 16.81 ± 2.38$^{**}$ |
| 3*C*40 | ... | ... | <1.11 | ... | ... | ... | ... | ... | <3.25 |
| 3*C*66*B*$^{*,b}$ | 0.0157 | 85.20 | 0.2081 | 0.053 | 250 | ... | ... | ... | 0.89 ± 0.23$^{*}$ |
| 3*C*83.1$^{*,c}$ | 0.0251 | 104.6 | 0.53 | 0.002 | – | 1.13 | 0.12 | 200 | 3.60 ± 0.0013 |
| 3*C*88$^{**,b}$ | 0.03 | 126.20 | 0.23 8 | 0.05 | 300 | ... | ... | ... | 2.19 ± 0.44$^{**}$ |
| 3*C*98 | ... | ... | <0.73 | ... | ... | ... | ... | ... | <7.27 |
| 3*C*129$^{*,c}$ | 0.0208 | 86.4 | 0.28 | 0.024 | – | 0.59 | 0.11 | 200 | 1.3 ± 0.11 |
| 3*C*236 | ... | ... | <0.75 | ... | ... | X | X | X | <80.70 |
| 3*C*264$^{**,a}$ | 0.02 | 90.90 | 0.70 | 0.15 | 200 | 1.48 | 0.16 | 225 | 3.37 ± 0.74$^{**}$ |
| 3*C*270 | ... | ... | <1.16 | ... | ... | ... | ... | ... | <0.69 |
| 3*C*272.1$^{*,a}$ | 0.0028 | 12.00 | 0.36 | 0.12 | 200 | 0.90 | 0.16 | 150 | 0.03 ± 0.01$^{*}$ |
| 3*C*274$^{**,b}$ | 0.0035 | 14.90 | 4.02 | 0.39 | 200 | ... | ... | ... | 0.52 ± 0.05$^{**}$ |
| 3*C*296 | ... | ... | <0.85 | ... | ... | ... | ... | ... | <5.05 |
| 3*C*305$^{**,b}$ | 0.042 | 171.70 | 1.19 | 0.14 | 600 | X | X | X | 20.52 ± 2.49$^{**}$ |
| 3*C*321$^{**,b}$ | 0.10 | 379.97 | 0.83 | 0.09 | 500 | X | X | X | 70.58 ± 7.93$^{**}$ |
| 3*C*327$^{*,b}$ | 0.1035 | 401.87 | 0.28 | 0.10 | 200 | X | X | X | 26.48 ± 9.59$^{*}$ |
| 3*C*353$^{**,b}$ | 0.0327 | 153.73 | 0.31 | 0.05 | 200 | ... | ... | ... | 4.27 ± 0.68$^{**}$ |
| 3*C*386$^{**,c}$ | 0.017 | 71.7 | 0.58 | 0.02 | — | 1.23 | 0.17 | 175 | 1.78 ± 0.058 |
| 3*C*402 | ... | ... | <0.95 | ... | ... | ... | ... | ... | <6.59 |
| 3*C*403$^{**,b}$ | 0.058 | 134.97 | 0.44 | 0.11 | 500 | X | X | X | 4.75 ± 1.18$^{**}$ |
| 3*C*433 | ... | ... | <0.87 | ... | ... | X | X | X | <93.13 |
| 3*C*442$^{**,c}$ | 0.0263 | 110.5 | 0.09 | 0.02 | — | 0.20 | 0.07 | 300 | 0.67 ± 0.16$^{**}$ |
| 3*C*449$^{**,b}$ | 0.0169 | 71.40 | 1.20 | 0.24 | 500 | ... | ... | ... | 3.59 ± 0.73 |
| 3*C*465 | ... | ... | <0.78 | ... | ... | ... | ... | ... | <7.69 |
| *NGC* 315$^{*,b}$ | 0.0175 | 73.80 | 0.26 | 0.06 | 150 | ... | ... | ... | 0.82 ± 0.19$^{*}$ |
| *NGC* 326$^{*}$ | 0.0474 | 203.18 | 0.2320 | 0.05 | 100 | 0.65 | 0.2 | 400 | 5.61 ± 1.2$^{*}$ |
| *NGC* 541$^{*,c}$ | 0.018 | 75.0 | 0.72 | 0.08 | 400 | 1.53 | 0.32 | 350 | 2.5 ± 0.27 |
| *NGC* 708$^{**,b}$ | 0.0166 | 69.86 | 1.84 | 0.31 | 600 | ... | ... | ... | 5.25 ± 0.88$^{**}$ |
| *NGC* 2484 | ... | ... | <1.00 | ... | ... | ... | ... | ... | <19.77 |
| *NGC* 2892 | ... | ... | <1.22 | ... | ... | ... | ... | ... | <6.85 |
| *NGC* 3801$^{**,b}$ | 0.0117 | 49.50 | 3.82 | 1.14 | 600 | ... | ... | ... | 5.49 ± 1.63$^{**}$ |
| *NGC* 4278$^{**,a*}$ | 0.0022 | 9.40 | 1.00 | 0.22 | 600 | 3.13 | 0.31 | 500 | 0.05 ± 0.01$^{**}$ |
| *NGC* 5127$^{**,c}$ | 0.016 | 67.1 | 0.28 | 0.02 | – | 0.59 | 0.10 | 100 | 0.79 ± 0.053 |
| *NGC* 5141 | ... | ... | <1.55 | ... | ... | ... | ... | ... | <5.04 |
| *NGC* 5490 | ... | ... | <1.92 | ... | ... | ... | ... | ... | <5.41 |
| *NGC* 6251 | ... | ... | <1.03 | ... | ... | X | X | X | <6.78 |
| *NGC* 7052$^{**,a}$ | 0.016 | 66.36 | 0.76 | 0.16 | 700 | 0.58 | 0.16 | 180 | 1.96 ± 0.41$^{**}$ |
| *B*2 0034 + 25 | ... | ... | <0.96 | ... | ... | ... | ... | ... | <10.41 |
| *B*2 0116 + 31$^{**,b}$ | 0.06 | 242.10 | 1.77 | 0.49 | 700 | 4.29 | 0.69 | 1000 | 60.63 ± 16.92$^{**}$ |
| *B*2 0648 + 27$^{**,a}$ | 0.04 | 169.83 | 0.72 | 0.07 | 300 | 1.44 | 0.34 | 350 | 12.25 ± 1.18$^{**}$ |
| *B*2 0836 + 29*B*$^{**,b}$ | 0.065 | 261.70 | 1.20 | 0.30 | 500 | X | X | X | 48.18 ± 11.95$^{**}$ |
| *B*2 0915 + 32*B* | ... | ... | <1.83 | ... | ... | ... | ... | ... | <70.52 |
| *B*2 0924 + 30$^{*,b}$ | 0.025 | 104.25 | 0.32 | 0.11 | 200 | ... | ... | ... | 2.01 ± 0.68$^{*}$ |
| *B*2 1101 + 38 | ... | ... | <1.35 | ... | ... | ... | ... | ... | <13.09 |
| *B*2 1347 + 28$^{*,b}$ | 0.072 | 297.9 | 0.35 | 0.08 | — | 0.75 | 0.25 | 500 | 17.04$^{*}$ |
| *B*2 1357 + 28 | ... | ... | <1.13 | ... | ... | ... | ... | ... | <48.09 |
| *B*2 1447 + 27 | ... | ... | <0.79 | ... | ... | ... | ... | ... | <7.96 |
| *B*2 1512 + 30 | ... | ... | <1.19 | ... | ... | ... | ... | ... | <110.54 |
| *B*2 1525 + 29 | ... | ... | <1.52 | ... | ... | ... | ... | ... | <69.55 |
| *B*2 1553 + 24 | ... | ... | <1.52 | ... | ... | ... | ... | ... | < 29.68 |
| *UGC*7115 | ... | ... | <1.53 | ... | ... | ... | ... | ... | <7.66 |
| *OQ*208$^{**,b}$ | 0.0766 | 304.90 | 2.51 | 0.33 | 400 | X | X | X | 136.51 ± 17.94$^{**}$ |

**Notes.** The $^{*}$ means that this galaxy is a tentative detection, the $^{**}$ means this galaxy is detected. The letter *a* is for (1-0)&(2-1) detected galaxies, *b* is for the CO(1-0) only detected galaxy and *c* is for the galaxies detected in CO(2-1) only; note that in this cases the velocity with is represented as **–** since the CO(1-0) value was calculated using the average of the ratio and therefore the width of the line is unknown. The case of NGC 4278, that has an $a^{*}$ is because this galaxy has been detected in (2-1) and tentatively detected in (1-0). In $M_{H_2}$ the $^{*}$ have the same meaning, only that in this case refers strictly to CO(1-0) since the integrated velocity for 3 mm was the one used to calculate the molecular mass.

### *3.2. CO(2-1)-to-CO(1-0) line ratios*

The line ratio of the CO(2-1) to the CO(1-0) transitions is computed by comparing the integrated intensity ratio of the lines $I_{CO(2\rightarrow1)}/I_{CO(1\rightarrow0)}$, where the intensity has been measured at one point at the center of each galaxy. Because of the different beam sizes for CO(1-0) and CO(2-1), the intensities should be compared only after obtaining small maps in CO(2-1) to sample the CO(1-0) beam. However, in most of our galaxies, the CO emission is expected to be almost a point source, at both

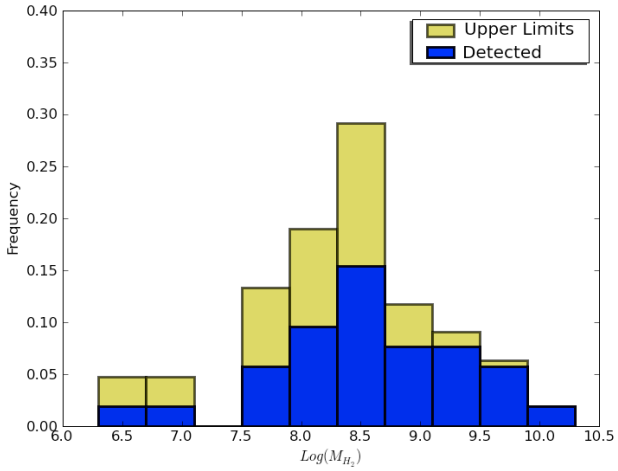


**Fig. 1.** This figure represents the $M_{H_2}$ histogram of the sample. The lighter color represents all the galaxies in the sample. Using ASURV, we were able to calculate the mass of the sample using both, upper limits and detected galaxies. Plotted at the bottom, with the darker color, are the detected galaxies only.

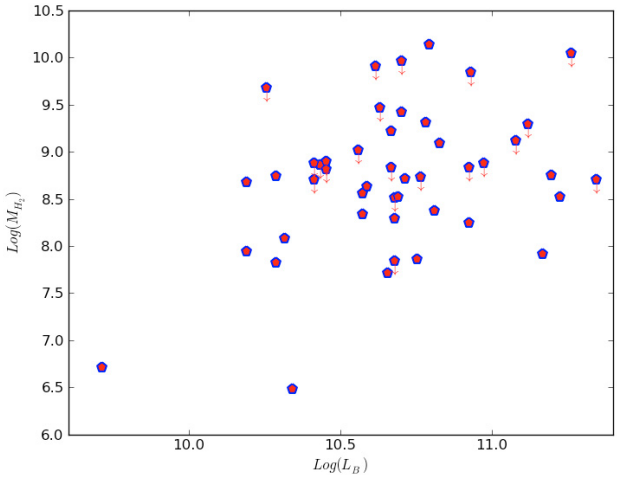


**Fig. 2.** Molecular gas mass versus blue luminosity with the upper limits for the molecular gas mass indicated.

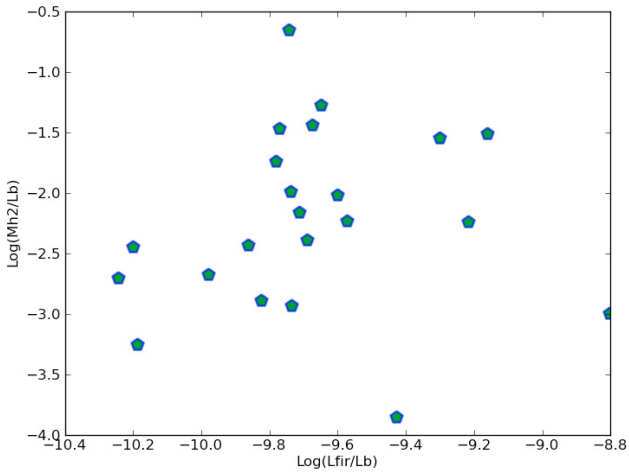


**Fig. 3.** Molecular gas mass versus FIR luminosity, both normalized by the blue luminosity, using only detected values.

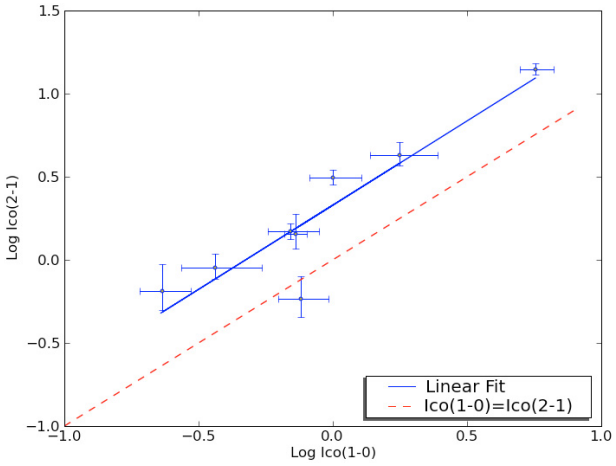


**Fig. 4.** Plot of the line ratio of the galaxies. The point that is outside of the linear fit is that of the galaxy NGC 7052.

frequencies. Except for NGC 4278, the distance of our detected galaxies is around or above 100 Mpc, where the CO(1-0) beam is 10 kpc, and in elliptical galaxies, the gaseous disks are expected to be, according to Young et al. (2008), concentrated in the nuclear disks on kpc scales. Therefore, equal $I_{CO}$ intensities in both lines will result in ratios of ∼4, the point-source dilution ratio of the two beams (for a more detailed derivation of beam couplings, see Appendix B).

As previously noticed by Lim et al. (2000), the 2 galaxies studied in their paper have a stronger observed intensity in CO(2-1) than in CO(1-0). This sample has a line ratio that greatly exceeds unity. Seven of our galaxies were detected at both frequencies and 6 more were detected only in CO(2-1). Of the galaxies detected at both frequencies, only NGC 7052 has an integrated intensity stronger in the CO(1-0) line than in the CO(2-1) line. The maximum line ratio was found to be 3.1 (for NGC 4278) and the average value 2.3±0.1. When correcting by the factor 4 of the beam dilution ratio, the average value is ∼0.6. This corresponds to an average over a moderate density disk, where most of the CO emission is optically thick, but sub-thermally excited. The maximum ratio obtained precisely for the most nearby galaxy NGC 4278 is 0.8, comparable to the typical value obtained for the central parts of spiral galaxies by Braine & Combes (1992).

Figure 4 plots the integrated intensity $I_{CO(2\rightarrow1)}$ versus (vs.) $I_{CO(1\rightarrow0)}$ and a line fit indicating a clear correlation. The dotted line in the plot represents intensities with the same value for both lines. Table 6 lists the line ratios for each galaxy (to see the spectra of those galaxies detected at both frequencies, see Fig. 15 of the online material, where the spectra of all galaxies in the sample are plotted). We note that the galaxy B2 0116+31 presents in its CO(1-0) line profile a strong absorption line, as well as the double line profile that can still be clearly seen. This absorption is the signature of molecular gas mass along the line of sight towards the AGN covering a very small area. Most of the radio galaxies observed have a radio continuum in millimeter strong enough to be detected in absorption, but in only one galaxy is the CO(1-0) transition absorbed toward the radio continuum. The double horn profile of B2 0116+31 is visible as well in the CO(2-1) transition line, where the absorption is much weaker, as well as the continuum at this frequency. The absorption line in this galaxy should cause an underestimation of the CO(1-0) integrated intensity and therefore an overestimate of the line ratio.

For galaxies detected in CO(2-1) emission line but not in CO(1-0), we derived a value for the integrated velocity $I_{CO(1-0)}$

**Table 6.** CO(2-1)-to CO(1-0) line ratio of the detected galaxies, not corrected by the different beam dilutions.

| Galaxy Name | Ratio |
|---|---|
| 3CR 31 | 2.5 ± 0.2 |
| 3CR 264 | 2.1 ± 0.2 |
| 3CR 272.1 | 2.5 ± 0.4 |
| NGC 326 | 2.8 ± 0.3 |
| NGC 4278 | 3.1 ± 0.4 |
| NGC 7052 | 0.8 ± 0.1 |
| B2 0116+31 | 2.4 ± 0.3 |
| B2 0648+27 | 2.0 ± 0.3 |

using the ratio of 2.3 calculated with the galaxies detected in both lines (for a closer view of the spectra of those galaxies, please see the online material, Fig. 15). The values of the derived molecular gas masses are already included in Table 5.

#### 3.2.1. Origin of the low line ratio

As mentioned previously, the observations were performed at only one point, at the center of the galaxies. However, the sources in the present sample are distant, and the expected extent of the CO emission is almost that of a point source, relative to the large CO beams. After deriving from either the HST optical images or the CO interferometric map of 3CR 31 (see Fig. C.2), the size of the molecular gas emission, we can correct for the beam/source coupling ratio. When considering the only 2 galaxies in this subsample for which we have the size of the molecular gas emission 3CR 31 (Sect. 3.4) and NGC 7052 (Sect. A), we could roughly say that the size of the galaxies varies from 4″ to 8″, so that the correction factor for this subsample would be between 0.25 and 0.35. For 3CR 31, the result is more accurate since we have the CO map from the PdBI, and as can be derived from the map, we can see the galaxy has a molecular gas size of about 8″, implying a correction factor of about 0.3. If the line ratio of 3C R31 is 2.5, then after the correction, the ratio would be 0.8. This value is lower than one, which may therefore indicate that the CO line is sub-thermally excited (Braine & Combes 1992). On average, we find a value of ∼0.6 for the CO(2-1)-to-CO(1-0) line ratio, which is compatible with that of a disk in which the CO line is optically thick and sub-thermally excited, as are the disks of spiral galaxies in general. Only when it is possible to resolve the center of the disk, in nearby galaxies has the ratio been observed to rise to 0.8–1 (Braine & Combes 1992).

### 3.3. Fanaroff and riley classification

Radio galaxies are divided into mainly two groups, the Fanaroff and Riley type I (FR-I) and type II (FR-II). As explained by Fanaroff & Riley (1974), the sources were classified using the ratio of the distance between the regions of highest brightness of the radio continuum on opposite sides of the central galaxy or quasar, to the total extent of the source measured from the lowest contour; those sources from which the ratio was less than 0.5 were placed in class I, and those for which the ratio was greater than 0.5 were placed in class II. There is a third classification called FR-c galaxies. These galaxies have very compact radio continuum emission.Their radio morphologies suggest that they are compact versions of the classical FR-II's, although why they are so small has not yet been established: they may be either young FR-IIs or FR-IIs trapped in a dense environment (Fanti et al. 1990; O'Dea et al. 1991; Fanti & Fanti 1994).

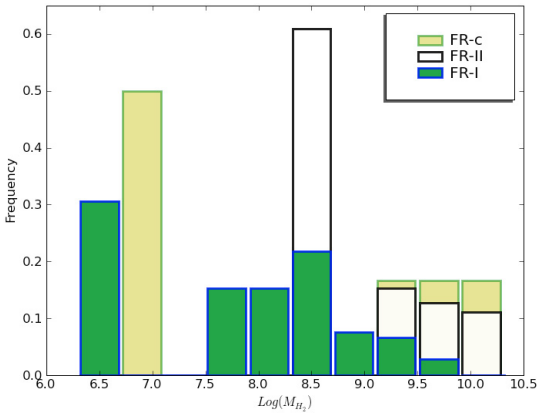


**Fig. 5.** Molecular gas mass distribution in the radio galaxies depending on their Fanaroff-Riley classification.

In the present sample, 69.2% are FR-I type galaxies, 19.2% are FR-II type galaxies, and 11.5% are FR-c type galaxies.

We previously found that the molecular gas mass average of our sample is $2.2 \times 10^8$ $M_\odot$. We found that FR-I and FR-II type galaxies behave differently from one another. The FR-II type galaxies have higher molecular gas masses than either the FR-I type galaxies or the FR-c type galaxies, as shown in Table 7, using the detected galaxies and the upper limits with the survival analysis statistics. The mean molecular gas mass is lower for the FR-I type galaxies than for the FR-II type galaxies, their values being $1.7 \times 10^8$ $M_\odot$ and $8.1 \times 10^8$ $M_\odot$, respectively. This difference is clearly visible in Fig. 5 where the molecular gas mass distribution is shown according to the types of radio galaxies: FR-I, FR-II, and FR-c. We can draw the following conclusions regarding the different types of radio galaxies and their molecular gas masses:

1. For the FR-I types, which contain the least powerful AGN, the elliptical host galaxy does not need much molecular gas mass to host the radio AGN. Molecular gas masses can be as low as $10^6$ $M_\odot$, which is a few giant molecular clouds (GMC).
2. For the median value of the molecular gas mass, FR-II type galaxies ($8.1 \times 10^8$ $M_\odot$) are clearly more massive than the FR-I ($1.98 \times 10^8$ $M_\odot$) and FR-c ($2.0 \times 10^7$ $M_\odot$) type galaxies. We note that there are only a few FR-c galaxies and therefore their statistical values are unreliable.

Evans et al. (2005) found only an 8% detection rate of CO emission in their FR-II galaxies, a very low value compared to the ∼35% detection rate of the FR-I detected in their sample. We also found a higher detection rate in FR-I galaxies than the FR-II galaxies. In our sample, the detection rate is 38.5% for FR-I, 11.5% for FR-II and 7.7% for FR-c galaxies. We note that the FR-II contain more powerful AGN, are rare and at larger distances compared to the other types found at larger distances. This can also explain both their lower detection rate, and their higher median molecular content.

To estimate more accurately the Malmquist bias in our sample, we plot in Fig. 6 the molecular gas mass vs. the redshift (z). It is clear that at higher z the galaxies tend to have higher molecular gas mass, because of the limits to the sensitivity of the telescope. The sensitivity limit was computed by assuming a typical value of 300 km s$^{-1}$ for the velocity width and 1 mK for the rms noise temperature. It is clear that there is a larger number of FR-II galaxies than either FR-I or FR-c galaxies at higher $z$, implying a higher threshold to the upper limit for the FR-II type

galaxies. This also agrees with the idea that FR-II galaxies are stronger AGN and more luminous, and this is also why they are seen at a greater distance. A factor 3 in the median mass can be expected, and we conclude that the difference between the radio galaxy types for the molecular gas mass could be caused only by the Malmquist bias.

### 3.4. Molecular gas disk

The double horn CO line profiles observed are characteristic of an inclined molecular gas rotating disk. In the present set of data, the double horn feature is present in 8 galaxies: 3CR 31, 3CR 264, 3CR 403, 3CR 449, NGC 3801, NGC 7052, B2 0116+31, and OQ 208, i.e., 29% of the detected galaxies in our sample. In the online material, Fig. 15, we present the spectra of those galaxies with a double horn profile. In the case of 3CR 31 and 3CR 264, the double horn profile is clearly visible in both transitions, CO(1-0) and CO(2-1), and for 3CR 403 and OQ 208 we see only this feature in the CO(1-0) transition since there is no data for the CO(2-1) transition. Five of the galaxies that present the double horn profile are FR-I types. Only one galaxy, 3CR 403, is an FR-II type, and two galaxies, OQ 208 and B2 0116+31, are FR-c type.

We also note that 4 of our 8 galaxies were detected in both transitions (3CR 31, 3CR 264, NGC 7052, and B2 0116+31) and in all 4 cases the CO(2-1) line is stronger than the CO(1-0) line (more details about the line ratios of these galaxies are given in Sect. 3.2).

The galaxies with the double horn profiles feature also have the highest $H_2$ masses. The average value for this subsample is $29.1 \times 10^8$ $M_\odot$, an order of magnitude higher than the average value for the complete sample of detected galaxies only ($2.2 \times 10^8$ $M_\odot$).

In some cases, we note that the absorption of the CO transitions could mimic a double horn profile. It appears from the peak temperature in the double horn profiles that in all cases, except for the CO(2-1) emission in 3CR 31, the double horn profile could be perturbed by an absorption line.

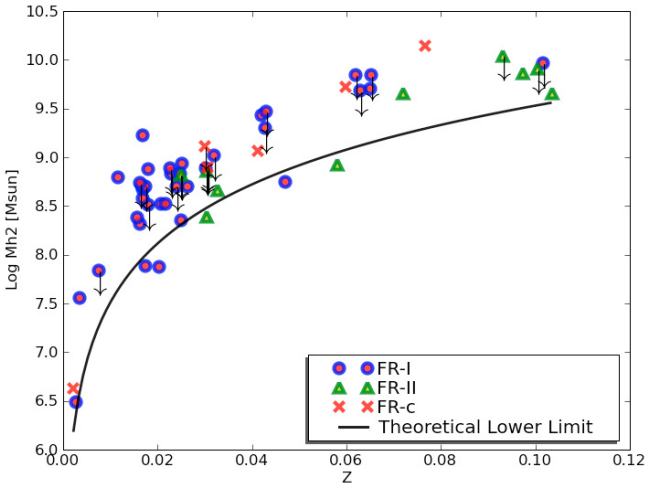


**Fig. 6.** $M_{H_2}$ versus $z$ and a lower limit of the theoretical value for the mass with respect to the distance.

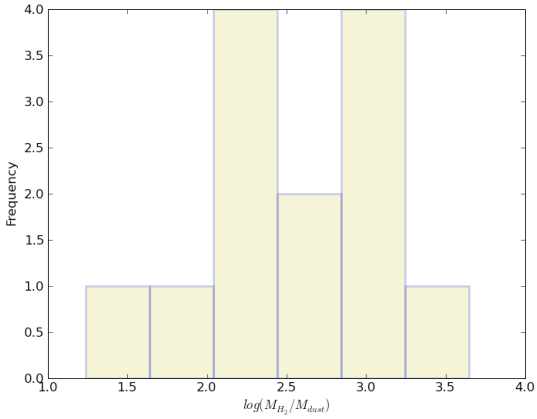


**Fig. 7.** Histogram of the Gas-to-Dust mass ratio.

## 4. Dust

Dust is an important ingredient of the ISM, associated with the molecular gas. It is heated by stars and/or an AGN, and its FIR emission depends strongly on its temperature, giving information about star formation (SF) in the galaxies. We analyze the dust emission at 60 $\mu$m and 100 $\mu$m in our sample. The fluxes at these frequencies allow us to estimate the temperature and the mass of the warm dust component. In a companion paper, we use the fluxes at 12 $\mu$m and 25$\mu$m as well as the fluxes from the Spitzer satellite using both cameras, IRAC (3.6, 4.5, 5.8, 8 $\mu$) and MIPS (24,70, 160 $\mu$m) to create the spectral energy distribution (SEDs) and study in more detail the synchrotron and thermal emission in each galaxy of the sample.

The dust temperature $T_d$ is calculated by adopting a modified black-body emissivity law

$$S_\nu \propto \kappa_\nu B_\nu(T_d), \quad (7)$$

where $\kappa_\nu$ is the dust emissivity and $B_\nu(T_d)$ is the Planck function at the dust temperature $T_d$. We then calculate the dust mass to be

$$M_{dust} = 4.78 f_{100} D_L^2 (e^{(143.88/T_d)} - 1)\ M_\odot, \quad (8)$$

where $f_{100}$ is the flux at 100 $\mu$m in Jy, $D_L$ the luminosity distance in Mpc, and $T_d$ the dust temperature in K. For this sample, the median value of the dust temperature using the galaxies detected by IRAS, is 35.8 K and the median value of the dust mass for the sample, only for the galaxies detected by IRAS, is $2.5 \times 10^6$ $M_\odot$. The detailed list of values for each detected galaxy at the frequencies of 60 $\mu$m and 100 $\mu$m is given in Table 9.

Using the galaxies detected with both IRAS and IRAM-30m, the $M_{H_2}/M_{dust}$ gas-to-dust mass ratio for this sample is 260. In Fig. 7, the distribution of the gas-to-dust mass ratio is shown, where the galaxies range between 20 and 4450 in terms of gas-to-dust mass ratio. Comparing with the sample that includes the upper limits for the molecular gas mass gives us an upper limit for the ratio of 254 on average. Figure 8a is the histogram of the dust mass of this sample. We note that most of the galaxies in this sample have a dust mass in the range $7.4–30 \times 10^5$ $M_\odot$ with 80% of the detected galaxies having a dust mass greater than $7.4 \times 10^5$ $M_\odot$. The dust temperature is mostly between 27.0 and 34.4 K (see Fig. 8b), although there are 2 galaxies with estimated dust temperatures of 64 and 71.4 K, respectively. These 2 galaxies, which hence have a hotter dust component than the others, are 3CR 327 and B2 0648+29B. These temperatures are derived assuming that the heated dust is mainly radiated by the FIR traced by the IRAS fluxes at 60 and 100 $\mu$m. Nevertheless, we cannot discard a contribution from warmer and colder dust components than traced by IRAS. This issue will be addressed in a companion paper.

**Table 7.** Mean and median values of the molecular gas mass of all subsamples separately in logarithmic values in units of $M_\odot$.

| | Detected & Upper Limits | | Detected only | |
|---|---|---|---|---|
| **Galaxy Name** | **Mean** | **Median** | **Mean** | **Median** |
| **FR-I** | $1.7 \times 10^8\ ^{+2.3\times10^8}_{-1.2\times10^8}$ | $1.86 \times 10^8$ | $2.3 \times 10^8\ ^{+3.2\times10^8}_{-1.6\times10^8}$ | $2.01 \times 10^8$ |
| **FR-II** | $8.1 \times 10^8\ ^{+1.22\times10^9}_{-5.3\times10^8}$ | $4.45 \times 10^8$ | $1.1 \times 10^9\ ^{+1.7\times10^9}_{-6.5\times10^8}$ | $4.6 \times 10^8$ |
| **FR-c** | $2.1 \times 10^8\ ^{+9.2\times10^8}_{-4.8\times10^7}$ | $2.03 \times 10^7$ | $8.5 \times 10^8\ ^{+4.0\times10^9}_{-1.8\times10^8}$ | $1.2 \times 10^9$ |
| **Total** | $2.3 \times 10^8\ ^{+3.2\times10^8}_{-1.68\times10^8}$ | $2.2 \times 10^8$ | $3.7 \times 10^8\ ^{+5.2\times10^8}_{-2.6\times10^8}$ | $3.4 \times 10^8$ |

## 5. FIR vs. CO

### 5.1. FIR & CO Luminosity

We calculated the CO(1-0) line luminosity, $L'_{\rm CO}$, which is expressed as the product of the velocity-integrated source brightness temperature, $T_{\rm b}\Delta V$, and the source area $\Omega_s D_{\rm A}^2$, to have for our sample in a mean value of $4.2 \times 10^7$ K kms$^{-1}$ pc$^2$. This value was calculated using ASURV for the upper limits. The CO(1-0) luminosity mean value is $6.4 \times 10^7$ K km s$^{-1}$ pc$^2$ calculated only with the detected values of the CO(1-0) emission lines. Taken from Solomon et al. (1997), the formula used for the calculation is

$$L'_{\rm CO} = 23.5 \times \Omega^2_{s*b} D_{\rm L}^2 I_{\rm CO}(1+z)^{-3}, \quad (9)$$

where $\Omega_{s*b}$ is the solid angle of the CO(1-0) emission for the source convolved with the telescope beam, $D_{\rm L}$ the distance in Mpc, $I_{\rm CO}$ is the integrated velocity in K km s$^{-1}$ (in $T_{\rm mb}$), and z the redshift of the galaxy. If the source is smaller than the beam, which is the case for all the galaxies in this sample, we can assume that $\Omega_{s*b} \approx \Omega_{\rm b}$ given in arcsec$^2$. The $L_{\rm FIR}$ is the far-IR luminosity which uses the fluxes at 60 and 100 $\mu$m, where the 60 $\mu$m flux density is associated with the warmer component and the 100 $\mu$m flux density is associated with cooler components. It was computed using the following relation from Sanders & Mirabel (1996)

$$L_{\rm FIR} = \left[1 + \frac{f_{100}}{2.58 f_{60}}\right] L_{60}, \quad (10)$$

where $f_{60}$ and $f_{100}$ are the fluxes at 60 and 100 $\mu$m, respectively, in units of Jy, and $L_{60}$ is the luminosity at 60 $\mu$m in $L_\odot$ represented as

$$\log(L_{60}) = 6.014 + 2\log(D) + \log(f_{60}), \quad (11)$$

where D is the distance of the galaxy in Mpc.

The results can be seen in Table 10 for which the median value of $L_{\rm FIR} = 6.9 \times 10^9\ L_\odot$. This value was calculated using ASURV to take into account the upper limits.

### 5.2. Star formation

The ratio $L_{\rm FIR}/L'_{\rm CO}$ is normally related in spiral galaxies to the star formation efficiency (SFE). This assumes that most of the FIR emission originates in the dust heated by young stars. In the case of powerful AGN, there is always the possibility of an added FIR contribution from dust heated by the AGN in a dusty torus. However, this contribution is rarely dominant (see e.g., Genzel & Cesarsky 2000). Figure 9 is a plot of the galaxies in our sample that illustrates the $L_{\rm FIR}$ vs. $L'_{\rm CO}$ relationship for the detected galaxies in both FIR and CO with their error bars, the galaxies with upper limits, represented by arrows (e.g., down arrow is for the CO upper limit and FIR detection, right arrow is for the CO detected and upper limits for the FIR, and the diagonal arrows are for the CO and FIR upper limits) the green line with the two circles indicate when the $L_{\rm FIR}$ was calculated with a 60 $\mu$m flux detection and 100 $\mu$m flux upper limit, which represent the lower and upper limit for $L_{\rm FIR}$. The linear relation between $L_{\rm FIR}$ and $L'_{\rm CO}$ is $\log(L'_{\rm CO}) = 0.8\log(L_{\rm FIR}) + 0.1$ with a $\chi^2$ of 0.024. Finally, the relationship itself has a median value for the $L_{\rm FIR}/L'_{\rm CO}$ ratio of about 52 $L_\odot$ (K km s$^{-1}$ pc$^2$)$^{-1}$.

We note that the detection rate for both FIR and CO together is independent of the type of radio galaxy. Out of the 15 radio galaxies detected in both FIR and CO, 8 (22%) are FR-I (3CR 31, 3CR 272.1, 3CR 274, 3CR 305, NGC 315, NGC 708, NGC 7052 and B2 0836+29B), 3 (30%) are FR-II (3CR 88, 3CR 321 and 3CR 327), and 4 (66%) are FR-c (NGC 4278, B2 0116+31, B2 0648+27 and OQ 208). We also note that of the 15 galaxies detected in both FIR and CO, only 4 have a double-horn profile feature (3CR 31, NGC 7052, B2 0116+31, and OQ 208).

As mentioned before $L_{\rm FIR}/L'_{\rm CO}$ is interpreted as a measure of the SFE. The star formation rate (SFR) per unit gas mass, according to Gao & Solomon (2004), is represented as

$$\dot{M}_{\rm SFR} \approx 2 \times 10^{-10}\ (L_{\rm FIR}/L_\odot) M_\odot\ {\rm yr}^{-1}. \quad (12)$$

From this estimation, we compute a mean SFR for this sample of about $3.7 \pm 1.5\ M_\odot$/yr, assuming that all the FIR emission comes from the dust heated by the young formed stars. This is likely an overestimation since it does not take into account the AGN heating of the dust.

### 5.3. CO-FIR relationship

In systems with ongoing star formation (SF), the light from both newly formed and older stars can be absorbed by dust and reprocessed into the FIR. Bell (2003) states that since young stars in HII regions heat dust to relatively high temperatures (with a low 100 $\mu$m-to-60 $\mu$m ratio of about ~1), we should be able to determine the origin of the IR emission, and this ratio leads to a wide range in $f_{100\ \mu{\rm m}}/f_{60\ \mu{\rm m}}$ on galaxy-wide scales, from ~10 for early-type spiral galaxies to $\lesssim$1 for the most intensely star-forming galaxies suggesting that earlier types are influenced by old stellar populations.

Our sample has a median value of $f_{100\ \mu{\rm m}}/f_{60\ \mu{\rm m}} = 1.9$ with its smaller value being 0.55 for 3C 327, which could be interpreted as a galaxy with a high temperature heated up by young stars in HII regions. Its highest value is 4.5 for 3CR 88, which is, still, a small value compared to ~10 for quiescent early-type spirals suggested by Bell (2003).

Figure 9 shows a linear relation in our data between $L'_{\rm CO}$ and $L_{\rm FIR}$. It is evident that the CO luminosities increase linearly with increasing $L_{\rm FIR}$, following a relation $\log(L'_{\rm CO}) = 0.8\log(L_{\rm FIR}) - 0.6$. In the plot, we can see two linear fits, the first one, the solid line, represents the linear fit to the galaxies for this sample only.

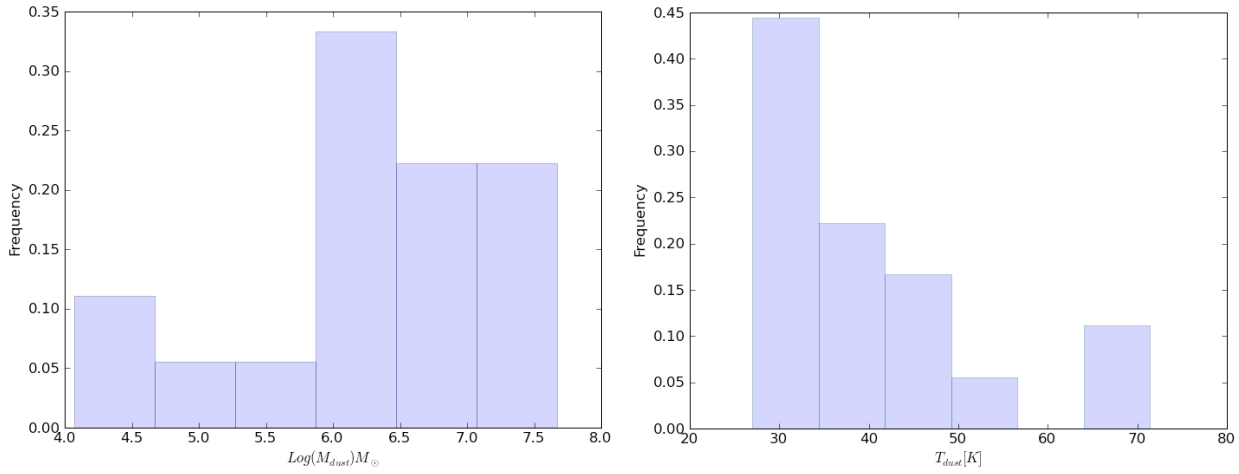


(a) (b)

**Fig. 8.** Histograms of the dust characteristic of the sample. Figure **a)** is the dust mass in logarithmic values and Fig. **b)** is the dust temperature.

**Table 8.** Molecular mass gas of the galaxies that exhibit a double horn profile.

| **Galaxy** | $M_{H_2}$ ($\times 10^8$ $M_\odot$) |
|---|---|
| 3CR 31 | 16.81 ± 2.38 |
| 3CR 264 | 3.37 ± 0.74 |
| 3CR 403 | 4.75 ± 1.18 |
| 3CR 449 | 3.59 ± 0.73 |
| NGC 3801 | 5.49 ± 1.63 |
| NGC 7052 | 1.96 ± 0.41 |
| B2 0116+31 | 60.63 ± 16.92 |
| OQ 208 | 136.51± 17.94 |
| **Average value:** | 29.14 ± 5.24 |

**Table 9.** Dust mass and temperature.

| **Galaxy Name** | $\log(M_{dust})$ ($M_\odot$) | $T_{dust}$ (K) |
|---|---|---|
| 3C31 | 6.8 | 28.3 |
| 3C88 | 7.1 | 27.0 |
| 3C272.1 | 4.6 | 36.4 |
| 3C274 (M87) | 4.1 | 47.4 |
| 3C305 | 6.4 | 39.5 |
| 3C321 | 7.1 | 50.8 |
| 3C327 | 6.4 | 71.3 |
| 3C402 | 7.0 | 27.8 |
| NGC 315 | 5.5 | 42.9 |
| NGC 708 | 6.3 | 29.7 |
| NGC 4278 | 5 | 20 |
| NGC 6251 | 6.9 | 30 |
| NGC 7052 | 6.2 | 34.1 |
| B2 0116+31 | 7.4 | 29.2 |
| B2 0648+27 | 6.2 | 68.5 |
| B2 0836+29B | 6.8 | 42.8 |
| B2 1101+38 | 6.2 | 35.3 |
| OQ 208 | 7.2 | 41.2 |

In Sect. 6, we compare our sample with other samples, this second fit, the dashed line, being the fit that we obtained by fitting all the galaxies together.

We related the line ratio of the galaxies clearly detected in both lines to the gas-to-dust mass ratio as can be seen in the online section in Fig. B.1. From this, we see that most of the galaxies have a gas-to-dust mass ratio lower than the median value for the ratio of the complete sample. We recall that the average gas-to-dust mass ratio of the sample is ∼300.

The galaxy 3CR 88 has the lowest gas-to-dust mass ratio, 17, a very low value compared to NGC 4278 with a ratio of 600. We also considered the relation between SFE ($L'_{CO}/L_{FIR}$) and $L_B$, as shown in Fig. 10, finding no correlation at all. In the figures the triangles are for the FR-I type galaxies, the squares are for the FR-II and the circles for the FR-c. The sample all together do not show correlations as well as all the subsamples separately.

## 6. Comparison with other samples

### 6.1. General description of the comparison samples

We compare our sample with other samples selected based on different criteria.

– Evans et al. (2005) observed a sample of elliptical radio galaxies, similar to our own but selected with the IRAS fluxes densities at 60 $\mu$m, $f_{60\ \mu m}$, or 100 $\mu$m, $f_{100\ \mu m}$, greater than 0.3 Jy, since they assumed that this level is a good indicator of a dusty, gas-rich, interstellar medium.

– Wiklind et al. (1995) observed a sample of elliptical galaxies selected on the basis of their morphological type. They argue that there is a major difficulty in defining a sample of elliptical galaxies because of their uncertain morphological classification. According to them, the most robust criterion for defining an elliptical galaxy appears to be the Vaucouleurs $r^{1\backslash 4}$ luminosity profile, and based on this, they selected genuine ellipticals, or galaxies that had a consistent classification as $E$ in several catalogs. A 100 $\mu$m flux $\gtrsim$1 Jy and $\delta > 0°$ were an additional criterion.

– Mazzarella et al. (1993) studied an infrared limited sample with 60 $\mu$m flux greater than 0.3 Jy. The objects were chosen to fully cover the sky, and to be relatively nearby ($z < 0.1$), with no other selection criteria.

– Bertram et al. (2007) studied a sample of galaxies hosting low-luminosity quasi-stellar objects (QSOs) for which they argue that an abundant supply of gas is necessary to fuel both

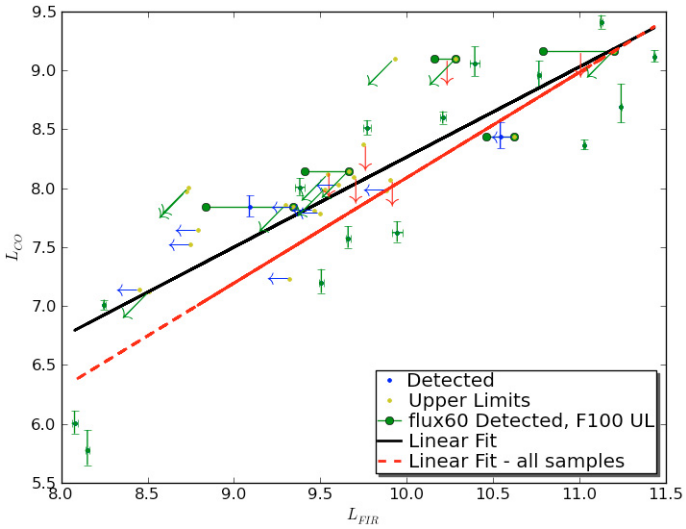


**Fig. 9.** $L_{\rm FIR}$ vs. $L'_{\rm CO}$ for the galaxies in this sample. Note that the arrows represent the upper limits: those pointing down correspond to the upper limit of $L_{\rm CO}$, those pointing left to that of $L_{\rm FIR}$, and those pointing in a southwest direction to the upper limits of $L_{\rm CO}$ and $L_{\rm FIR}$. We also show cases where $f_{60}$ is considered a detection and $f_{100}$ an upper limit. Cases such as these are represented by a line with 2 circles at the edges for the lower and upper limits for $L_{\rm FIR}$. When $L_{\rm CO}$ is a detection, the error bars are shown centered on the line; on the other hand, when $L_{\rm CO}$ is an upper limit, it is indicated by an arrow pointing down.

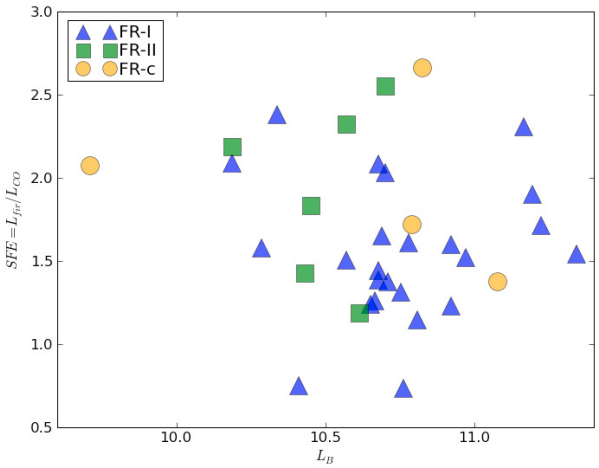


**Fig. 10.** Star formation efficiency compared to the blue luminosity of this sample of galaxies. Note that the triangles are for the FR-I type galaxies, the squares are for the FR-II and the circles for the FR-c.

an active galactic nucleus and any circumnuclear starburst activity. The only criterion for selection was their small cosmological distance: only objects with a redshift $z < 0.060$ were chosen.

– Solomon et al. (1997) studied a sample of 37 infrared-luminous galaxies in the redshift range $z = 0.02$–$0.27$. Eleven of these galaxies have a 60 $\mu$m flux $S_{60} > 5.0$ Jy, and are part of the near bright galaxy sample (Sanders et al. 1988, 1991). Twenty galaxies were chosen from a redshift survey (Strauss et al. 1992) of all IRAS sources with 60 $\mu$m fluxes $S_{60} > 1.9$ Jy. A few lower luminosity sources were also included in the sample.

**Table 10.** Values of CO(1-0) luminosities and FIR luminosities.

| **Galaxy** | $\log(L'_{\rm CO})$ (K km s$^{-1}$ pc$^2$) | $\log(L_{\rm FIR})$ ($L_\odot$) |
|---|---|---|
| 3C31 | 8.51 | 9.77 |
| 3C40 | <7.86 | <9.30 |
| 3C66B | 7.23 | <9.32 |
| 3C83.1 | 7.78 | <9.50 |
| 3C88 | 7.62 | 9.94 |
| 3C98 | <8.12 | <9.54 |
| 3C129 | 7.38 | ... |
| 3C264 | 7.81 | <9.46 |
| 3C270 | <7.13 | <8.51 |
| 3C272.1 | 5.77 | 8.23 |
| 3C274 | 7.01 | 8.25 |
| 3C296 | <7.99 | <9.53 |
| 3C305 | 8.60 | 10.21 |
| 3C321 | 9.12 | 11.43 |
| 3C236 | <9.10 | <10.28 |
| 3C327 | 8.69 | 11.24 |
| 3C353 | 7.80 | ... |
| 3C386 | 7.52 | <8.75 |
| 3C402 | <8.07 | 9.90 |
| 3C403 | 8.43 | <10.62 |
| 3C433 | <9.17 | <11.20 |
| 3C442 | 7.08 | ... |
| 3C449 | 7.84 | <9.34 |
| 3C465 | <8.14 | <9.66 |
| NGC 315 | 7.20 | 9.51 |
| NGC 326 | 7.98 | <9.88 |
| NGC 541 | 7.64 | <8.79 |
| NGC 708 | 8.01 | 9.38 |
| NGC 2484 | <8.54 | ... |
| NGC 2892 | <8.10 | ... |
| NGC 3801 | 8.03 | <9.60 |
| NGC 4278 | 6.00 | 8.08 |
| NGC 5127 | 7.14 | <8.45 |
| NGC 5141 | <7.97 | <8.72 |
| NGC 5490 | <8.00 | <8.74 |
| NGC 6251 | <8.09 | 9.69 |
| NGC 7052 | 7.58 | 9.65 |
| B2 0034+25 | <8.27 | ... |
| B2 0116+31 | 9.06 | 10.39 |
| B2 0648+27 | 8.37 | 11.03 |
| B2 0836+29B | 8.96 | 10.76 |
| B2 0915+32B | <9.10 | <9.93 |
| B2 0924+30 | 7.59 | ... |
| B2 1101+38 | <8.37 | 9.75 |
| B2 1347+28 | 8.50 | ... |
| B3 1357+28 | <8.90 | ... |
| B3 1447+27 | <8.16 | ... |
| B3 1512+30 | <9.23 | ... |
| B3 1525+29 | <9.06 | ... |
| B3 1553+24 | <8.72 | ... |
| UGC 7115 | <8.19 | ... |
| OQ 208 | 9.41 | 11.12 |

### 6.2. Molecular gas mass

Comparing our sample with the others mentioned above, we noticed that those of Wiklind et al. (1995) and ourselves sample have an average molecular gas mass of a few $10^8$ $M_\odot$ (using only detected galaxies, not the survival analysis median value) and that both samples are hosted by elliptical galaxies. The Mazzarella et al. (1993), Evans et al. (2005) and Bertram et al. (2007) samples all have a median molecular gas mass value of about $10^9$ $M_\odot$, their samples are FIR selected galaxies or galaxies in interaction, therefore they are expected to have higher

molecular gas mass than in the sample hosted by normal elliptical galaxies. They conclude that the majority of luminous, low-redshift QSOs have gas-rich host galaxies. We note that of all galaxies in our sample the QSO, OQ 208, is the galaxy with the highest molecular gas mass ($1.4\times10^{10}\ M_{\odot}$). Finally the sample of Solomon et al. (1997) has the highest average molecular gas mass of $10^{10}\ M_{\odot}$, being a sample of ULIRGs in which intense star formation is occurring. Table 12 compares the average molecular gas masses with those of other samples, and the characteristics of the various samples.

We note that when we compare our sample with the others, we use the median value for the molecular gas mass that was calculated using only the detected galaxies for consistency with the other studies where the upper limits were not used in the calculations.

If we now compare with a subsample of galaxies from TANGO itself that were detected in both IRAS (for 60 $\mu$m and 100 $\mu$m) and CO(1-0), we have a total of 15 galaxies with a median value of $1.22\times10^{9}\ M_{\odot}$. This is an order of magnitude higher than the median value of molecular gas mass for the complete sample. It is in complete agreement with the statement that galaxies with higher FIR fluxes have more molecular gas mass than galaxies that are dimmer in their FIR emission.

### 6.3. Molecular gas disk

Double-horned CO profiles have been previously noted by several authors. We compare the fraction of double-horn CO profile in our sample with the fraction in other samples. For instance, Evans et al. (2005) detected a double-horn CO emission line profile in many of the spectra. Out of nine detected galaxies, 5 exhibit a double-horn profile. They studied two different cases for which they had interferometric data, finding in the first case that this was caused by a CO absorption feature at the systemic velocity of the galaxy (Evans et al. 1999) and in the other case, for 3CR 31, that the molecular gas is distributed in a molecular gas disk (Okuda et al. 2005). Wiklind et al. (1995) found one case of double-horn profile out of 4 galaxies detected. Bertram et al. (2007) found 11 double-horn among their 26 detected galaxies and Mazzarella et al. (1993) 2 out of 4 galaxies detected with the double-horn profile. In Table 13, we give the percentage of molecular gas disk traced by the double horn profile for each sample. Similarely as for the molecular gas properties, the closest sample to our radio galaxy sample is that of Wiklind et al. (1995), which is composed of genuine elliptical galaxies. Thus it seems that the presence or not of a radio source is independent of the molecular gas properties, on the kpc scale, of the host elliptical galaxy. The FIR-selected samples have a higher percentage of molecular gas disk than the sample selected only on the basis of the radio continuum properties. The dispersion value in the percentage of molecular gas disks in each sample was computed using Poissonian statistics.

We add that we do not discard the possibility that the double horn profile in these galaxies might be caused by projection effects (i.e., inclination of the galaxy onto the sky plane).

### 6.4. Dust

We also compare the dust properties in our sample of radio galaxies, hosted by elliptical galaxies, with the sample of elliptical galaxies from Wiklind et al. (1995) (see Figs. 8 and 11). The dust component in our sample is slightly hotter than in the comparison sample of Wiklind et al. (1995) with a median value of 34 K. The median value of the gas-to-dust mass ratio for Wiklind et al. (1995) is 700, much higher than the median value of the ratio in our sample, which is close to 260. Evans et al. (2005) found a gas-to-dust mass ratio even higher with a median value of 860. The sample of low luminosity QSOs (from Bertram et al. 2007) has a lower ratio of 452 and Mazzarella et al. (1993) with their sample of radio galaxies detected by IRAS has a higher gas-to-dust mass ratio of 506.

### 6.5. CO vs. FIR

The sample of Solomon et al. (1997), which is composed of ULIRGs, is the sample with the highest value of $L_{\rm FIR}/L'_{\rm CO}$ at 146 $L_{\odot}$(K km s$^{-1}$ pc$^{2}$)$^{-1}$. According to Solomon & Sage (1988), this implies that this group of galaxies are strongly interacting/merging galaxies with a strong SF, although this is mainly for spiral galaxies and we cannot use this study to classify the remaining galaxies here. Our sample has a ratio of 52, which is quite different from the ratio of 39 in the elliptical galaxies observed by Wiklind et al. (1995). Both Evans et al. (2005) and Wiklind et al. (1995) measure similar ratios, Evans et al. (2005) a ratio of 35. Bertram et al. (2007) find a ratio of 49.1 and finally Mazzarella et al. (1993) a very high ratio of 82.

In Table 11, we indicate the median values of the CO(1-0) and FIR luminosity for the comparison samples and the median value of the star formation efficiency (SFE=$L_{\rm FIR}/L'_{\rm CO}$). As already known, (see e.g., Gao & Solomon 2004), the ULIRG sample of Solomon et al. (1997) has the highest SFE indicator value of 147. With a median $L_{\rm FIR}$ value of $1.94\times10^{11}$, the sample of radio galaxies of Mazzarella et al. (1993) exhibits a high SFR probably tracing the star formation in merger galaxies. Similarly to the ULIRG sample, the sample of Mazzarella et al. (1993) have a quite high SFE indicator (82). The sample of low luminosity QSO host galaxies from Bertram et al. (2007) as well as the galaxies in this sample, were chosen without any bias towards the FIR emission and their SFE values appear to be similar at 49 and 52, respectively. Finally, the samples of elliptical galaxies (Wiklind & Henkel 1995) and FIR-selected radio galaxies (Evans et al. 2005) have low values of the SFE indicator of 39 and 35, respectively.

The CO vs. FIR luminosity diagram is used in spiral galaxies to relate a tracer of the molecular gas, the CO emission, to a tracer of the star formation, the FIR emission. We compared the $L_{\rm FIR}$ vs. $L'_{\rm CO}$ relationship in our sample with that in other samples.

A linear regression was fitted to the entire set of data (see Fig. 12) and individual samples. The linear regression is then $\log(L_{\rm CO}) = m.\log(L_{\rm FIR}) + b$, where $m = 0.9$ and $b = -0.9$ have a mean square error of 0.43. Considering the samples all together, we obtain a $\chi^2 = 0.022$.

Since our data are well fitted by the CO-FIR relationship compared to the other samples, we can argue that the radio galaxies hosted by the elliptical galaxies should exhibit at least a low level of star formation.

Apart from the samples aforementioned, in Fig. 12 we include 3 more samples: Young et al. (1995), Young et al. (1996), and a sample of spiral galaxies observed as part of the FCRAO Extragalactic CO survey. We also include the sample of Braine & Combes (1992), composed of spiral galaxies. These samples were used to add well-defined samples to the study of the CO-FIR relationship since the star formation completely dominates that relationship in spiral galaxies.

**Table 11.** FIR-to-CO luminosities and their ratios.

| Sample name | $L_{FIR}$ ($L_\odot$) | $L'_{CO}$ (K km s$^{-1}$ pc$^2$) | $L_{FIR}/L'_{CO}$ ratio. ($L_\odot$(K km s$^{-1}$ pc$^2$)$^{-1}$) |
|---|---|---|---|
| This sample | $8.9 \times 10^9$ | $4.2 \times 10^7$ | 52.0 |
| Wiklind et al. (1995) | $6.5 \times 10^9$ | $1.6 \times 10^8$ | 39.4 |
| Mazzarella et al. (1993) | $1.94 \times 10^{11}$ | $1.1 \times 10^9$ | 82.2 |
| Evans et al. (2005) | $3.6 \times 10^{10}$ | $1.2 \times 10^9$ | 35.4 |
| Bertram et al. (2007) | $4.2 \times 10^{10}$ | $9.2 \times 10^8$ | 49.1 |
| Solomon et al. (1997) | $1.2 \times 10^{12}$ | $7.9 \times 10^9$ | 146.8 |

**Table 12.** Comparison samples and the median value of their molecular gas masses.

| Criteria of selection | Sample name | Molecular gas mass ($\times 10^8$ $M_{H_2}$) |
|---|---|---|
| **Elliptical galaxies** | This sample | 3.7 |
| | Wiklind et al. (1995) | 6.8 |
| **FIR galaxies and QSO's** | Evans et al. (2005) | 37 |
| | Mazzarella et al. (1993) | 11 |
| | Bertram et al. (2007) | 30 |
| **ULIRGS** | Solomon et al. (1997) | 100 |

## 7. Discussion

As we have shown, the molecular gas content of the host elliptical galaxies of powerful radio-AGN appears to be low compared to spiral galaxies. The origin of that gas can either be internal (stellar mass loss, cooling gas from a galaxy halo of hot gas) or external (minor/major merger, accretion-fed from cosmological filaments, cooling flows), when the radio galaxy is at the center of a cluster. Salomé et al. (2008) provide an exhaustive discussion of the molecular gas in cooling flow that can be accreted by an elliptical galaxy. We estimate the stellar mass loss $\eta$ by using the B magnitude of the elliptical host (Athey et al. 2002), namely $\eta = 0.0078(M_\odot/10^9\ L_{\odot,B})\ M_\odot$/yr. Figure 14 shows the distribution of the stellar mass loss in our sample of radio galaxies detected in CO or with an upper limit of molecular gas mass lower than $5\times10^9\ M_\odot$ to constrain the stellar mass loss contribution. The median value of the stellar mass loss is 0.37 $M_\odot$.yr$^{-1}$. This value implies that a median time of 1 Gyr is required to refurbish the galaxy with molecular gas provided by the stellar mass loss without taking into account the consumption rate of the AGN (e.g., David et al. 2006). As shown in Fig. 13, a substantial fraction of radio galaxies have a filling time $M(H_2)/\eta$ of molecular gas provided by the stellar mass loss over a timescale longer than 1 Gyr (36%), reaching timescales close to the age of the Universe. With the accretion rate of the radio-AGN (see e.g. Lagos et al. 2009) it allows us to discard the stellar mass loss as a mechanism sufficient for providing the molecular gas in these elliptical galaxies. In other words, we would expect the gas lost by the stars to be hot and to enrich the hot halo gas by means of a stellar wind, in spheroidal galaxies, thir spherical geometry diluting the gas, such that the density is never high enough to cool. The cooling time begins after 10 Gyr, so most of this gas remains hot and will not be detected in $H_2$/CO. This is not the case for spiral galaxies where the gravity and density are stronger so that the gas can cool to the HI-$H_2$ phase.

If the molecular gas in the radio galaxies were provided by the stellar mass loss, we would expect, to first order, the molecular gas mass to correlate with the blue luminosity, a proxy of the galaxy stellar mass.That hypothesis is discarded by the data in Fig. 2. The external hypothesis for the origin of the molecular gas is more likely to explain a large part of the molecular gas present in the elliptical galaxies hosting radio AGN. Lim et al. (2000) favored the minor merger scenario for the origin of the molecular gas in 3CR 31 because of its smooth isophotes that show no signs of recent perturbations caused by a major merger. However, 3CR 31 is the brightest galaxy in a cluster with a cooling flow (Crawford et al. 1999).

**Table 13.** Percentage of the galaxies, within the detected galaxies of each sample of the double horn CO profile feature.

| Sample | Molecular gas disk (%) | Dispersion (%) |
|---|---|---|
| This sample | 27.6 | 9.4 |
| Wiklind et al. (1995) | 25 | 25 |
| Mazzarella et al. (1993) | 50 | 35 |
| Evans et al. (2005) | 55.6 | 25 |
| Bertram et al. (2007) | 42.3 | 13 |

The inspection of the optical images shows that several radio galaxies are in dense environments where the minor/major mergers should be frequent enough to deposit molecular gas within the elliptical galaxies. The accretion of gas from cosmological filaments has been studied by numerical simulations (Dekel et al. 2009) and should be an additional source of molecular gas in these galaxies.

In the case of 3CR 31, there are suggestions, by Martel et al. (1999), that the galaxy is interacting. Baldi & Capetti (2008) suggest that 3C 264 has no young stellar population. Emonts et al. (2006) propose that B2 0648+27 formed from a major merger event that occurred $\lesssim$ 1.5 Gyr ago. García-Burillo et al. (2007) state that the distortions in B2 0116+31 may indicate that the disk is still settling after a merger or gas accretion event, or maybe the jet and the cone-line features might be interacting with the disk to produce the reported distortion. For NGC 4278 Giroletti et al. (2005) state that its central BH is active and able to produce jets; however, the lifetime of its components of <100 yr at the present epoch, combined with the lack of large-scale emission, suggests that the jets are disrupted before they reach kiloparsec scales. In conclusion, the origin of the gas in these galaxies may be multiple, the majority also being external, and a composite scenario can be invoked for each galaxy.

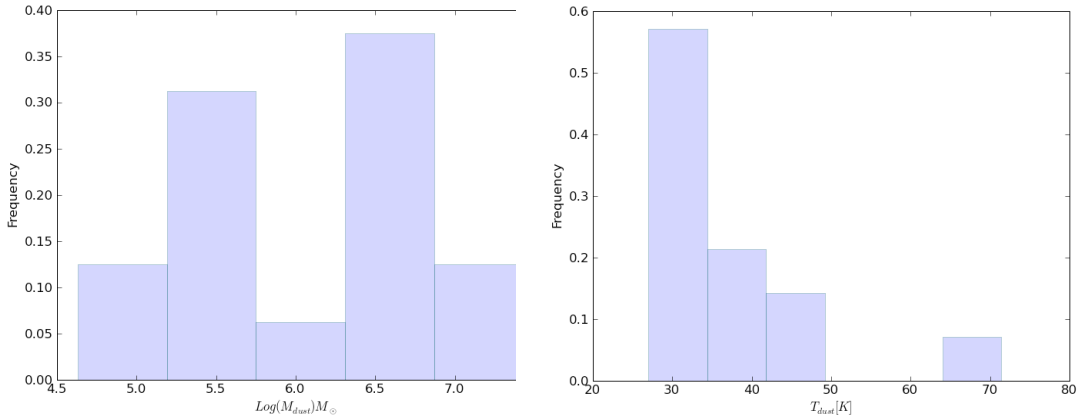


(a) (b)

**Fig. 11.** Histograms of the dust mass and the dust temperature of the sample of Wiklind et al. (1995). **a)** is the distribution of the logarithmic mass; and **b)** is the distribution of the temperature.

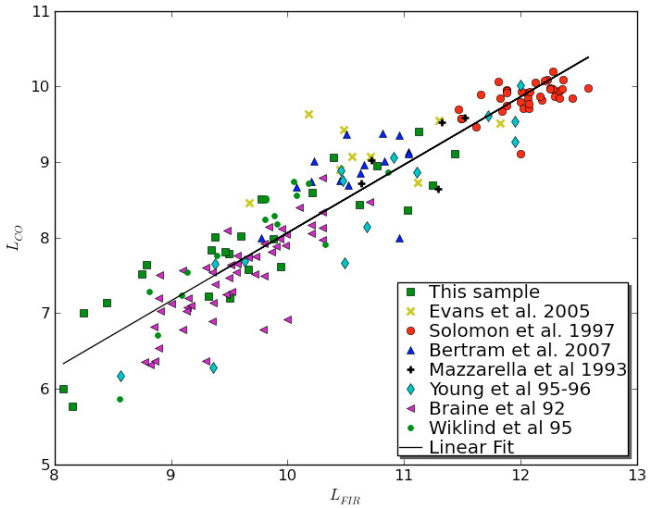


**Fig. 12.** $L_{\rm FIR}$ vs. $L'_{\rm CO}$ of all the samples used in this paper. As can be appreciated from this plot, galaxies from Solomon et al. (1997), which are ULIRGs, are are more closely fit by the linear fit, as expected from the information in Table 11.

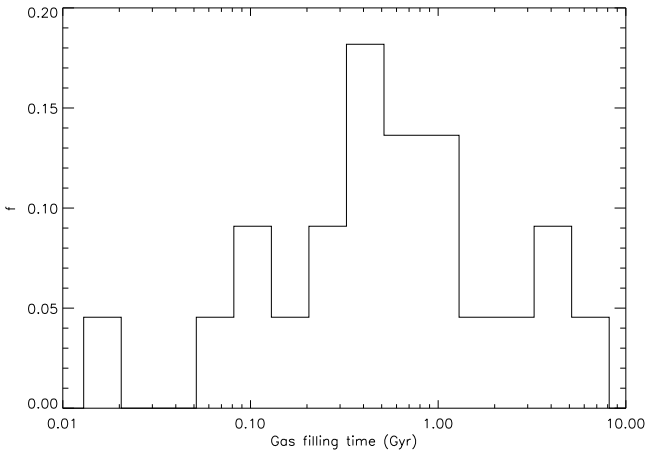


**Fig. 13.** Histogram of the gas filling time for our sample.

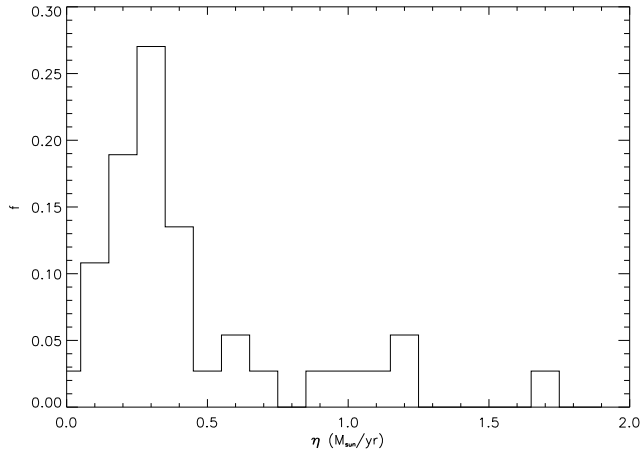


**Fig. 14.** Histogram of the stellar mass loss in $M_\odot$/yr for our sample of radio galaxies.

## 8. Summary and conclusions

We have presented a survey of CO(1-0) and CO(2-1) lines for 52 radio galaxies in the Local Universe selected only on the basis of their radio continuum emission:

- The detection rate is 38% (firm – 20/52), or 58% in total (30/52) when including tentative detections.
- An indication of a molecular gas disk (double-horn) is found in 15% of the galaxies (27% of the detected galaxies) with confirmation in 3CR 31 achieved using a PdBI CO(1-0) map.
- The CO(2-1)-to-CO(1-0) line ratio is 2.3 without taking into account beam dilution effect, and is likely to be ∼0.6 with corrections, which is indicative optically thick and sub-thermal CO emission.
- The low ratio of $f_{100}/f_{60}$ also suggests that this sample may be forming stars.

We compare the properties of our sample with different samples of elliptical galaxies, QSO and ULIRGs:

- We measured low molecular gas content compared to other selected samples, with a median value of $2.2 \times 10^8$ $M_\odot$.
- We confirm that FR-II type galaxies are characterized by lower CO detection rates than FR-I and FR-c radio sources as claimed by Evans et al. (2005), and that FR-IIs have a higher molecular gas mass, as expected for the existing Malmquist bias in this sample.

– The $L_{\rm FIR}$ vs. $L'_{\rm CO}$ relation is similar to that found in the other samples suggesting that some star formation could be occurring in these elliptical radio galaxies.

*Acknowledgements.* We thank Eric Emsellem for a careful refereeing and a detailed report, which helped to improve this paper significantly. B. Ocaña Flaquer and S. Leon are partially supported by DGI Grant AYA2008-06181-C02-02, Spain. We thank Pamela Ocaña for her careful readings and inputs on the manuscript.

## References

Allen, S. W., Dunn, R. J. H., Fabian, A. C., Taylor, G. B., & Reynolds, C. S. 2006, MNRAS, 372, 21
Antonucci, R. 1993, ARA&A, 31, 473
Athey, A., Bregman, J., Bregman, J., Temi, P., & Sauvage, M. 2002, ApJ, 571, 272
Baars, J. W. M. 1973, IEEE Trans. Ant. Prop, 461, 21
Baldi, R. D., & Capetti, A. 2008, A&A, 489, 989
Baum, S. A., O'Dea, C. P., Giovannini, G., et al. 1997, ApJ, 483, 178
Bell, E. F. 2003, ApJ, 586, 794
Bennett, A. S. 1962, MmRAS, 68, 163
Bertram, T., Eckart, A., Fischer, S., et al. 2007, A&A, 470, 571
Best, P. N., Kaiser, C. R., Heckman, T. M., & Kauffmann, G. 2006, MNRAS, 368, L67
Braine, J., & Combes, F. 1992, A&A, 264, 433
Butcher, H. R., van Breugel, W., & Miley, G. K. 1980, ApJ, 235, 749
Colla, G., Fanti, C., Ficarra, A., et al. 1970, A&AS, 1, 281
Colla, G., Fanti, C., Fanti, R., et al. 1972, A&AS, 7, 1
Colla, G., Fanti, C., Fanti, R., et al. 1973, A&AS, 11, 291
Combes, F. 2002, ArXiv Astrophysics e-prints
Combes, F., Young, L. M., & Bureau, M. 2007, MNRAS, 377, 1795
Crane, P., Peletier, R., Baxter, D., et al. 1993, ApJ, 402, L37
Crawford, C. S., Allen, S. W., Ebeling, H., Edge, A. C., & Fabian, A. C. 1999, MNRAS, 306, 857
David, L. P., Jones, C., Forman, W., Vargas, I. M., & Nulsen, P. 2006, ApJ, 653, 207
de Rijcke, S., Buyle, P., Cannon, J., et al. 2006, A&A, 454, L111
de Ruiter, H. R., Parma, P., Capetti, A., Fanti, R., & Morganti, R. 2002, A&A, 396, 857
Dekel, A., Sari, R., & Ceverino, D. 2009, ApJ, 703, 785
Dreyer, J. L. E. 1888, MmRAS, 49, 1
Edge, D. O., Shakeshaft, J. R., McAdam, W. B., Baldwin, J. E., & Archer, S. 1959, MmRAS, 68, 37
Emonts, B. H. C. 2006, Ph.D. Thesis, Groningen University
Emonts, B. H. C., Morganti, R., Tadhunter, C. N., et al. 2006, A&A, 454, 125
Evans, A. S., Sanders, D. B., Surace, J. A., & Mazzarella, J. M. 1999, ApJ, 511, 730
Evans, A. S., Mazzarella, J. M., Surace, J. A., et al. 2005, ApJS, 159, 197
Fanaroff, B. L., & Riley, J. M. 1974, MNRAS, 167, 31P
Fanti, C., & Fanti, R. 1994, in The Physics of Active Galaxies, ed. G. V. Bicknell, M. A. Dopita, & P. J. Quinn, ASP Conf. Ser., 54, 341
Fanti, C., Fanti, R., Ficarra, A., & Padrielli, L. 1974, A&AS, 18, 147
Fanti, R., Fanti, C., Schilizzi, R. T., et al. 1990, A&A, 231, 333
Gao, Y., & Solomon, P. M. 2004, ApJ, 606, 271
García-Burillo, S., Combes, F., Neri, R., et al. 2007, A&A, 468, L71
Genzel, R., & Cesarsky, C. J. 2000, ARA&A, 38, 761
Giroletti, M., Taylor, G. B., & Giovannini, G. 2005, ApJ, 622, 178
Gordon, M. A., Baars, J. W. M., & Cocke, W. J. 1992, A&A, 264, 337
Hardcastle, M. J., Kraft, R. P., Worrall, D. M., et al. 2007, ApJ, 662, 166
Heisler, C. A., & Vader, J. P. 1994, AJ, 107, 35
Jackson, N., Sparks, W. B., Miley, G. K., & Macchetto, F. 1995, A&A, 296, 339
Kellermann, K. I., & Verschuur, G. L. 1988, Galactic and extragalactic radio astronomy (2nd edn) (Galactic and Extragalactic Radio Astronomy)
Kennicutt, Jr., R. C. 1998, ARA&A, 36, 189
Knapp, G. R., Guhathakurta, P., Kim, D., & Jura, M. A. 1989, ApJS, 70, 329
Kramer, C. 1997, in Calibration procedures and efficiencies (IRAM)
Lagos, C. D. P., Padilla, N. D., & Cora, S. A. 2009, MNRAS, 397, L31
Lim, J., Leon, S., Combes, F., & Dinh-V-Trung. 2000, ApJ, 545, L93
Martel, A. R., Baum, S. A., Sparks, W. B., et al. 1999, ApJS, 122, 81
Mazzarella, J. M., Graham, J. R., Sanders, D. B., & Djorgovski, S. 1993, ApJ, 409, 170
Meng, D.-M., & Zhou, H.-Y. 2006, Chinese Journal of Astronomy and Astrophysics, 6, 25
Mihos, J. C., & Hernquist, L. 1994, ApJ, 437, 611
Mihos, J. C., & Hernquist, L. 1996, ApJ, 464, 641
Nieto, J.-L., McClure, R., Fletcher, J. M., et al. 1990, A&A, 235, L17
Nilson, P. 1973, Nova Acta Regiae Soc. Sci. Upsaliensis Ser. V, 0
Noel-Storr, J., Baum, S. A., Verdoes Kleijn, G., et al. 2003, ApJS, 148, 419
Northover, K. J. E. 1973, MNRAS, 165, 369
O'Dea, C. P., Baum, S. A., & Stanghellini, C. 1991, ApJ, 380, 66
Okuda, T., Kohno, K., Iguchi, S., & Nakanishi, K. 2005, ApJ, 620, 673
Rohlfs, K., & Wilson, T. L. 2004, Tools of radio astronomy (Tools of radio astronomy, 4th rev. and enl. ed., by K. Rohlfs and T.L. Wilson. (Berlin: Springer)
Salomé, P., & Combes, F. 2003, A&A, 412, 657
Salomé, P., Combes, F., Revaz, Y., et al. 2008, A&A, 484, 317
Sanders, D. B., & Mirabel, I. F. 1996, ARA&A, 34, 749
Sanders, D. B., Soifer, B. T., Elias, J. H., et al. 1988, ApJ, 325, 74
Sanders, D. B., Scoville, N. Z., & Soifer, B. T. 1991, ApJ, 370, 158
Sarzi, M., Falcón-Barroso, J., Davies, R. L., et al. 2006, MNRAS, 366, 1151
Scheer, D. J., & Kraus, J. D. 1967, AJ, 72, 536
Shlosman, I., Begelman, M. C., & Frank, J. 1990, Nature, 345, 679
Solomon, P. M., & Sage, L. J. 1988, ApJ, 334, 613
Solomon, P. M., Downes, D., Radford, S. J. E., & Barrett, J. W. 1997, ApJ, 478, 144
Strauss, M. A., Huchra, J. P., Davis, M., et al. 1992, ApJS, 83, 29
Strong, A. W., Bloemen, J. B. G. M., Dame, T. M., et al. 1988, A&A, 207, 1
Thi, W.-F., van Zadelhoff, G.-J., & van Dishoeck, E. F. 2004, A&A, 425, 955
Wiklind, T., & Henkel, C. 1995, A&A, 297, L71
Wiklind, T., & Rydbeck, G. 1986, A&A, 164, L22
Wiklind, T., Combes, F., & Henkel, C. 1995, A&A, 297, 643
Young, J. S., Xie, S., Tacconi, L., et al. 1995, ApJS, 98, 219
Young, J. S., Allen, L., Kenney, J. D. P., Lesser, A., & Rownd, B. 1996, AJ, 112, 1903
Young, L. M. 2002, AJ, 124, 788
Young, L. M., Bureau, M., & Cappellari, M. 2008, ApJ, 676, 317

Pages 16 to 23 are available in the electronic edition of the journal at http://www.aanda.org

## Appendix A: Individual galaxies

We present in various properties of the 29 detected galaxies, in order of increasing 3C numbers, then NGC and B2 numbers:

- **3C 31:** NGC 383, or Arp 331. For information on this galaxy, see Sect. 3.4.
- **3C 66b:** UGC 1841. The well known bright radio jet of this galaxy was first discovered by Northover (1973) and the optical jet was first detected by Butcher et al. (1980). Meng & Zhou (2006) were able to perform a detailed study of the jet using the HST/WFPC2 images comparing them with the high resolution radio images and finding excellent correspondence. The optical image detects a disk, which is consistent with the CO spectra of the galaxy. The detection is a very faint one. The central disk diameter is about 10″ in the optical image, and the CO velocity width is 250 km s$^{-1}$.
- **3C 83.1:** NGC 1265 (in Abell 426). It is one of the seven cases where the molecular gas was clearly detected in the CO(2-1) transition and not in the CO(1-0) transition. The optical image shows a dust lane of length 2.24″, according to Martel et al. (1999). This dust lane is oriented at ∼171°, nearly orthogonal to the radio jet. If the CO emission were to correspond to the dust lane, its small size could explain the CO(1-0) signal dilution and non-detection.
- **3C 88:** UGC 2748. It is clearly detected in the CO(1-0) transition. The optical image shows no peculiar feature.
- **3C 129:** It is another example of a CO(2-1) detection with an upper limit in the CO(1-0) line. The FWHM velocity width of this galaxy is 200 km s$^{-1}$. There is no hint of interaction in the Hubble image.
- **3C 264:** NGC 3862 (in Abell 1367). This galaxy has a double horn profile, in both transition lines, typical of a molecular gas disk (see Fig. 15). The velocity width of this galaxy is about 200 km s$^{-1}$. The disk profile can be seen in the optical image, which also reveals a jet (Crane et al. 1993). Baum et al. (1997) suggest that the optical synchrotron emission, clearly visible in the optical image from the HST, is associated with the jet. According to Martel et al. (1999), the nucleus is unresolved, and the host galaxy projected image is very circular and smooth.
- **3C 305:** IC 1065. In the CO(1-0) spectra, the detection is very clear, with a broad velocity width of ∼600 km s$^{-1}$. We have no data for the CO(2-1) emission line. The HST image presented by Martel et al. (1999) shows filamentary and disturbed swaths of dust stretching across the western side of the galaxy and a twisting "arm" of emission in the eastern side. Jackson et al. (1995) noticed a 1″scale cone-line extension of the continuum emission north of the core, in a direction almost 90° from the radio axis. They proposed that this might be an effect of obscuration of near-nuclear emission in all other directions rather than an example of scattering of anisotropic directed radiation from a hidden active nucleus.
- **3C 321:** The HST optical image shows an extended dust absorption in the galaxy. It is clearly detected in the CO(1-0) transition with a velocity width of ∼500 km s$^{-1}$. For the CO(2-1) emission, we have no data. The HST image reveals a nearby galaxy that might be interacting with this galaxy.
- **3C 327:** It is clearly detected in the CO(1-0) transition line, having a FWHM of ∼200 km s$^{-1}$ and one of the highest dust temperature in this sample (64 K).
- **3C 353:** It is clearly detected in the CO(1-0) transition line, with a velocity width of ∼200 km s$^{-1}$. Martel et al. (1999) propose that the outer isophotes of 3C 353 are very circular, while the inner isophotes are elongated in a southeast to northeast direction and are roughly peanut-shaped. Martel et al. (1999) also stated that this may be the result of a small-scale dust lane bifurcating the nucleus in a rough north-south direction or a true double nucleus.
- **3C 386:** It is clearly detected in CO(2-1) with a velocity width of ∼175 km s$^{-1}$, but not in CO(1-0). The HST optical image shows a bright optical nucleus where strong diffraction spikes dominate the core of the elliptical galaxy (Martel et al. 1999).
- **3C 403:** It is clearly detected in the only transition observed, CO(1-0), with a velocity width of ∼500 km s$^{-1}$. It presents the double horn profile already mentioned before and shown in Fig. 15. Martel et al. (1999) suggest this galaxy consists of two systems: a central elliptical region surrounded by a low-surface brightness halo with a sharp boundary at a distance of 3 kpc northwest of the nucleus. In the northwest region of the halo, two or three very weak dust lanes are barely discernible.
- **3C 442:** UGC 11958, Arp 169. Detected in the CO(2-1) emission line, but not in the CO(1-0). The HST optical image shows the elliptical shape of the galaxy but no evidence of dust obscuration. The isophotes of the outer halo of this elliptical galaxy are relatively smooth but within the central 520 pc, they are irregular and the light distribution becomes non-uniform.
- **3C 449:** It has a tentative double-horn profile that can be noticed from the CO(1-0) spectrum (Fig. 15), but one side is stronger than the other. From the HST image of this galaxy, it is possible to see the dust absorbing the visible light, not completely edge on. According to Martel et al. (1999), the morphology of this galaxy suggests that we are viewing the nearside of an inclined, geometrically thick torus or disk. The velocity width is about 500 km s$^{-1}$.
- **NGC 315:** It is detected in CO(1-0) only. There are no visible features in the HST image.
- **NGC 326:** Detected with a higher intensity in CO(2-1) than in CO(1-0).
- **NGC 541:** Arp 133 (in Abell 194). This galaxy was detected in CO(2-1) but not in CO(1-0). From the HST image, there is another galaxy that might be falling into NGC 541 and there is another larger galaxy probably having some tidal effects on NGC 541. According to Noel-Storr et al. (2003), this cD S0 galaxy has a radio core on VLBA scales and a core-jet morphology on VLA scales. The central isophotes, measured from the WFPC/2 images, vary considerably. The gas does not exhibit regular rotation profile.
- **NGC 708:** in Abell 262. Detected in CO(1-0) but not in CO(2-1). This is the central galaxy of a cooling flow cluster, detected by Salomé & Combes (2003).
- **NGC 3801:** It shows a double horn profile, detected in the CO(1-0) spectral line, with a velocity width of ∼600 km s$^{-1}$.
- **NGC 4278:** Also detected by Combes et al. (2007). The line emission is stronger in CO(2-1) than in CO(1-0), with a broader width. Note that this is the closest radio galaxy of all (9 Mpc). According to Combes et al. (2007), the dust morphology across the disk consists of irregular patches or lanes; this suggests that this galaxy has recently accreted its gas (Sarzi et al. 2006).
- **NGC 5127:** There is a clear detection in the CO(2-1) line. The dust absorption is not clearly visible in the HST image even though the galaxy is not so remote ($z = 0.016$).
- **NGC 7052:** It exhibits a double-horn profile very clear in the CO(1-0) emission (Fig. 15) but probably also in the CO(2-1) emission, although it is only a tentative detection there.

According to Nieto et al. (1990), the size of the dust disk is about 4″.

- **B2 0116+31:** This is a peculiar galaxy in this sample, showing a strong absorption line in CO(1-0). The molecular/dusty disk was studied in detail by García-Burillo et al. (2007) using the IRAM PdBI. The absorption line is surrounded by emission in both its blue and red-shifted wings. Because of the absorption, we cannot discard a possible double horn profile. As mentioned in Sect. 3.2, this absorption is the signature of molecular gas mass along the line of sight towards the AGN covering a very small area and because of its small filling factor, this absorption is quite rare, low, in contrast to that expected for a radio-selected sample. Its double-horn profile is also visible in the CO(2-1) transition line, where the absorption is much weaker; the continuum at this frequency is not detected, in contrast to the continuum for CO(1-0) which has a strong flux density of 164 mJy. The absorption line in this galaxy should cause an underestimation of the CO(1-0) integrated intensity and therefore an overestimation of the line ratio.
- **B2 0648+27:** It is detected in CO(1-0) & CO(2-1) with a line ratio of 2.82, the highest of all. Emonts (2006) observed this galaxy with the VLA-C, where they detected HI in both emission and absorption noting that it is distributed in a large and massive ring-like structure. The distribution and kinematics of the HI gas, the presence of faint tails in deep optical imaging (Heisler & Vader 1994), and the detection of a galaxy-scale post-starburst young stellar population, imply that this galaxy formed from a major merger event that happened ≥1.5Gyr ago.
- **B2 0836+29B:** It is clearly detected in the CO(1-0) emission line, but not in CO(2-1). There is nothing peculiar in its optical image.
- **B2 0924+30:** It shows a peculiar perturbed dust lane in the optical image that may have been caused by interactions. It was not detected in CO(2-1), although there is a clear detection of the CO(1-0) line. The HST image shows another smaller galaxy that might have fallen into B2 0924+30.
- **B2 1347+28:** in Abell 1800. Detected in the CO(2-1) line but not in CO(1-0). The disk in the optical image does not seem to be perfectly elliptical, maybe due to interactions.
- **OQ 208:** Mrk 668. It has only been observed in the CO(1-0) line and exhibits a clear double horn profile as shown in Fig. 15 with a velocity width of about 400 km s$^{-1}$.

## Appendix B: Beam/source coupling

To correct the observed emission line brightness temperatures for beam dilution, we assume that (Thi et al. 2004)

$$T'_{\rm MB} = \frac{T_{\rm MB}(\Omega_{\rm source} + \Omega_{\rm beam})}{\Omega_{\rm source}}, \quad \text{(B.1)}$$

where $T'_{\rm MB}$ is the true main beam temperature and $T_{\rm MB}$ is the observed main beam temperature. By assuming an axisymmetric source and beam distribution, we can represent their distribution by an angular $\theta$ parameter leading to a correction factor for the CO(2-1)-to-CO(1-0) line ratio of

$$K = \frac{\theta^2_{b-230} + \theta^2_{\rm s}}{\theta^2_{b-115} + \theta^2_{\rm s}}, \quad \text{(B.2)}$$

(see de Rijcke et al. (2006) for more details) where $\theta_{b-230}$ is the beam size at 230 GHz, $\theta_{b-115}$ is the beam size at 115 GHz, and

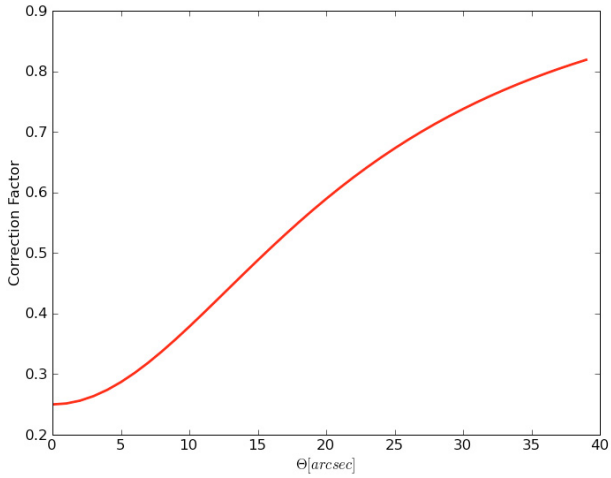


**Fig. B.1.** Correction factor K for the CO(2-1)-to-CO(1-0) line ration as a function of the size $\theta$ of the source detected in CO(1-0), to take into account the beam dilution. The possible sources go from a point like source to a source with a size of 22"

$\theta_{\rm s}$ is the angular size of the source. We recall that for a Gaussian beam $\Omega_{\rm beam} = \int_{\rm beam} P_\omega \omega {\rm d}\omega = \frac{1}{4ln2}\pi\theta^2_{\rm b} \simeq 1.133\theta^2_{\rm b}$, although the factor of 1.133 cancels out in Eq. (B.2). The correction factor K for the CO(2-1)-to-CO(1-0) line ratio is shown in Fig. B.1 as a function of the angular source size $\theta$, varying between 0.25, for a point source, and 1, for a completely extended source.

Besides to the galaxy 3CR 31, we did not apply the beam dilution correction because we do not know the molecular size of the galaxies and therefore the extent of the correction that we should apply.

## Appendix C: 3CR 31

This galaxy was observed in more details than the remaining galaxies. It is an FR-I radio galaxy at a distance of 71 Mpc hosted by an elliptical D galaxy in the Zwicky cluster 0107.5+3212. A double-horn profile of the CO(1-0) and CO(2-1) lines was found by Lim et al. (2000), giving a first indication of a central molecular gas disk (see Fig. C.3). The Nobeyama Millimeter Array (NMA) CO(1-0) interferometer observations by Okuda et al. (2005) confirmed the presence of this molecular gas disk. Our PdBI observations are about the same spatial resolution as the NMA ones but are of a higher sensitivity as shown by the CO(1-0) integrated intensity map in Fig. C.2. The mean surface density of the molecular gas in the center is found to be 340 $M_\odot$ pc$^{-2}$ given the spatial extension of 8″ for the molecular gas disk as shown on the CO(1-0) intensity profile along the major axis (see Fig. C.1).

From the PdBI image (see Fig. C.1 and C.2), we know that the molecular gas extension in 3CR 31 is about 8″. Applying the correction factor for the beam dilution (see Fig. B.2) to the CO(2-1)-to-CO(1-0) line ratio of 2.47 found with the IRAM-30m observations, the true line ratio would decrease to 0.8 assuming that the CO(2-1) component is 8″ large. According to Braine & Combes (1992), a line ratio of about 0.7 implies an optically thick gas with an excitation temperature of about 7 K. Figure C.4 shows the position-velocity (PV) diagram for the CO(1-0) emission in 3CR 31. We can see that at 1″, the maximum velocity is $V_{\rm max} = 190$ km s$^{-1}$. Applying the correction for the inclination ($i = 39°$), the maximum rotation velocity at a radius of 1″ is $V_{\rm rot_{max}} = V_{\rm max}/\sin(i) = 317$ km s$^{-1}$. Thus the dynamical mass inside a radius of 1″is estimated using

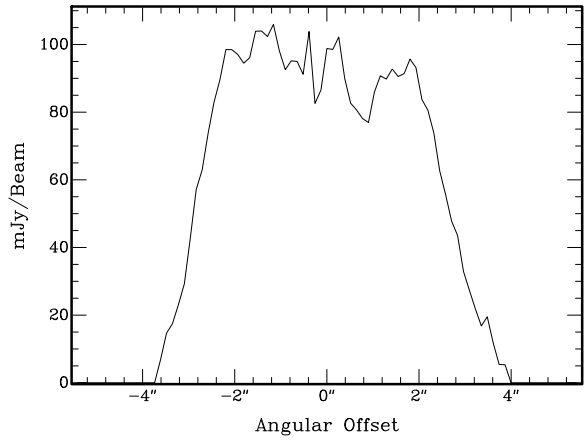


**Fig. C.1.** CO(1-0) intensity profile along the major axis for the 3CR 31 galaxy.

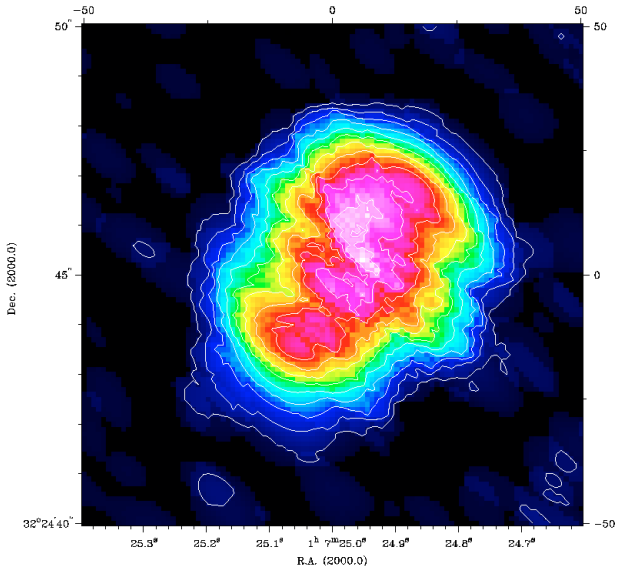


**Fig. C.2.** CO(1-0) map of the PdBI for the 3CR 31 galaxy.

$M_{\rm dyn} = \frac{R*V_{\rm rot}^2}{G} = 1.02\times10^{10}\ M_\odot$. We estimate the total molecular gas mass inside a radius of 1″ to be $1.04\times10^8\ M_\odot$ using the mean surface gas density, therefore the molecular gas represents about 1% of the dynamical mass at the very center of 3CR 31. Okuda et al. (2005) discussed in detail the dynamical and stability implications for the molecular gas at the center of 3CR 31.

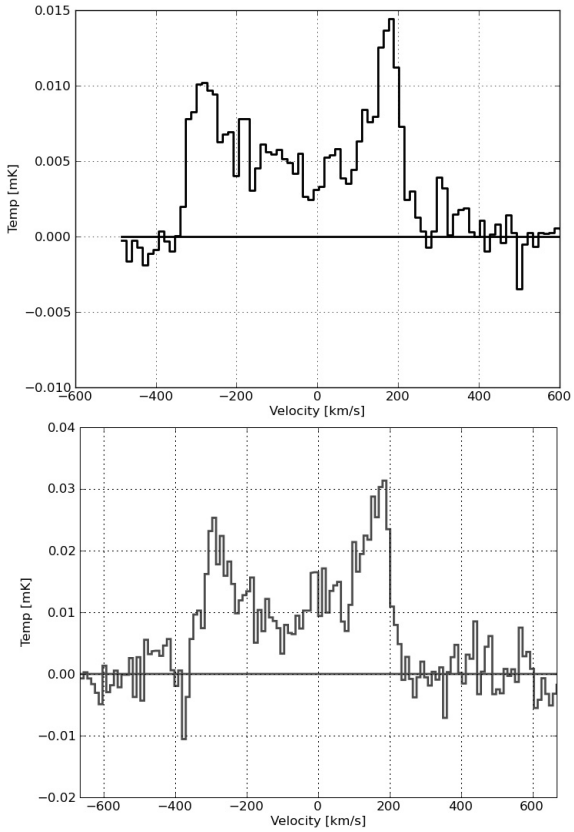


**Fig. C.3.** 3CR 31 spectra of the CO(1-0) (upper image) and CO(2-1) (lower image) lines.

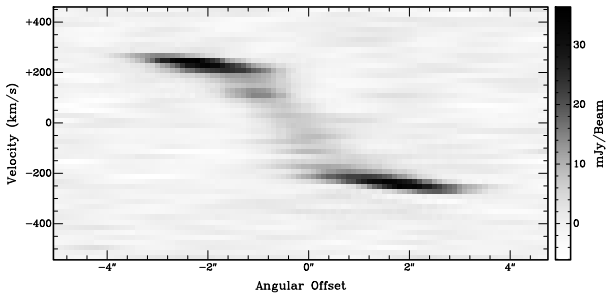


**Fig. C.4.** PV-diagram along the major axis for the CO(1-0) emission in the 3CR 31 galaxy from the PdBI data.

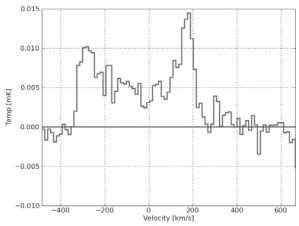


3CR 31 CO(1-0)

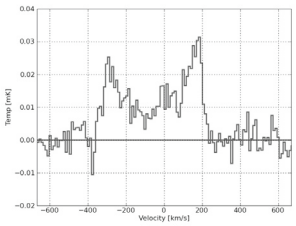


3CR 31 CO(2-1)

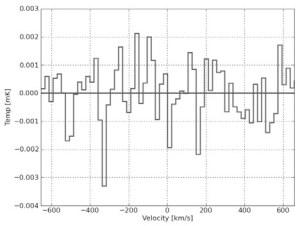


3CR 40 CO(1-0)

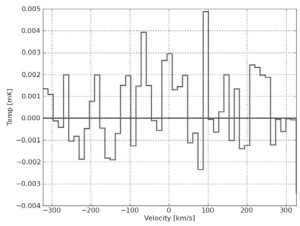


3CR 40 CO(2-1)

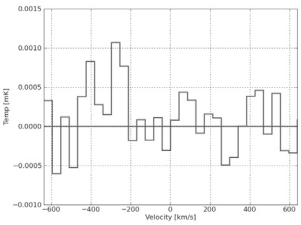


3CR 66B CO(1-0)

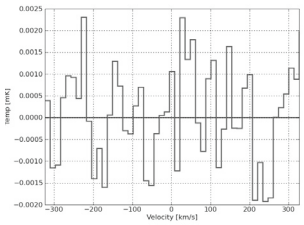


3CR 66B CO(2-1)

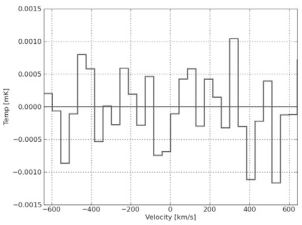


3CR 83.1 CO(1-0)

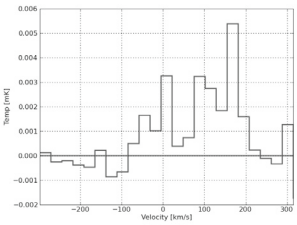


3CR 83.1 CO(2-1)

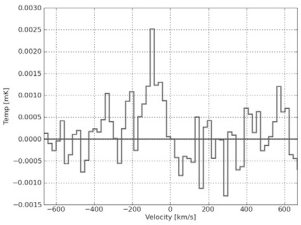


3CR 88 CO(1-0)

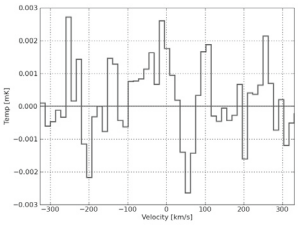


3CR 88 CO(2-1)

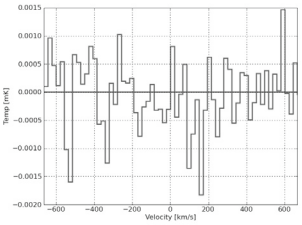


3CR 98 CO(1-0)

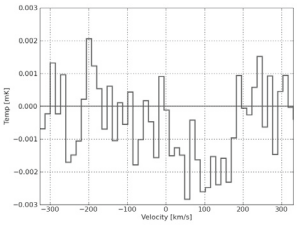


3CR 98 CO(2-1)

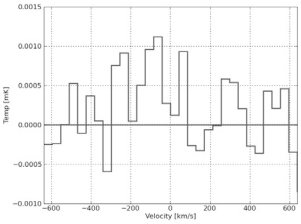


3CR 129 CO(1-0)

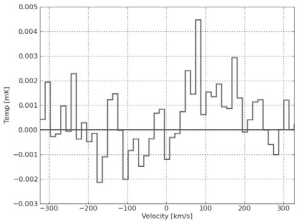


3CR 129 CO(2-1)

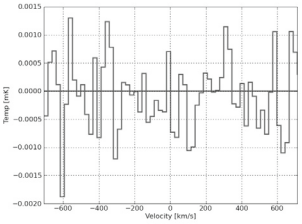


3CR 236 CO(1-0)

NO DATA AVAILABLE

3CR 236 CO(2-1)

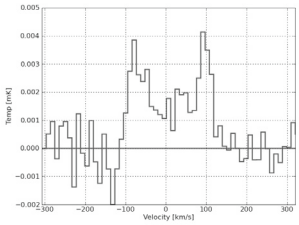


3CR 264 CO(1-0)

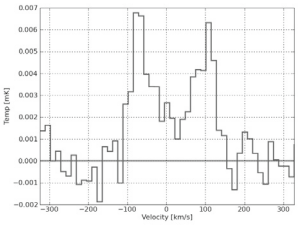


3CR 264 CO(2-1)

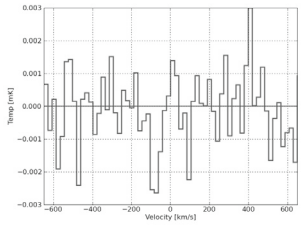


3CR 270 CO(1-0)

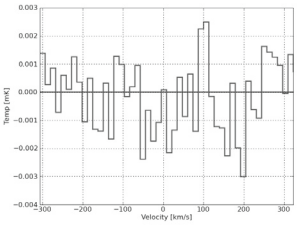


3CR 270 CO(2-1)

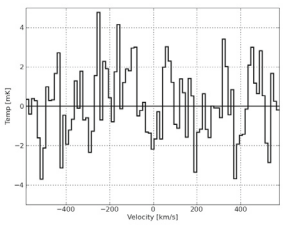


3CR 272.1 CO(1-0)

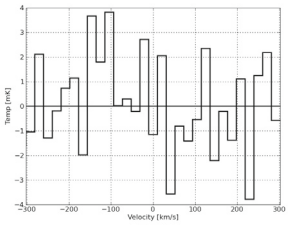


3CR 272.1 CO(2-1)

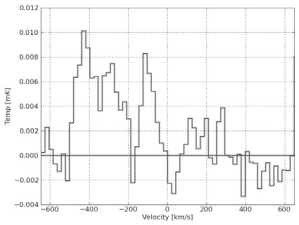


3CR 274 CO(1-0)

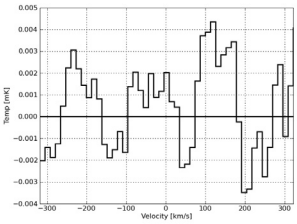


3CR 274 CO(2-1)

**Fig. 15.** Spectra of all the galaxies in the sample.

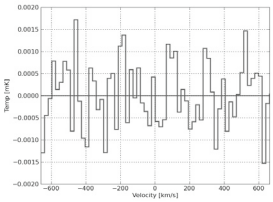

3CR 296 CO(1-0)

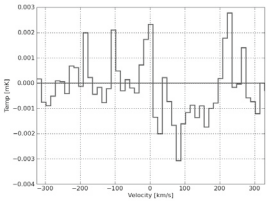

3CR 296 CO(2-1)

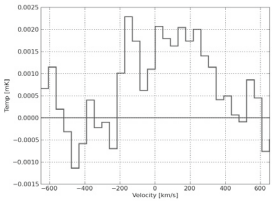

3CR 305 CO(1-0)

NO DATA AVAILABLE

3CR 305 CO(2-1)

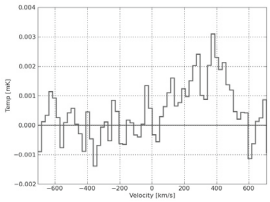

3CR 321 CO(1-0)

NO DATA AVAILABLE

3CR 321 CO(2-1)

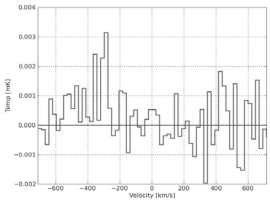

3CR 327 CO(1-0)

NO DATA AVAILABLE

3CR 327 CO(2-1)

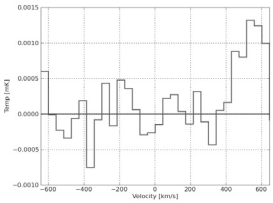

53CR 353 CO(1-0)

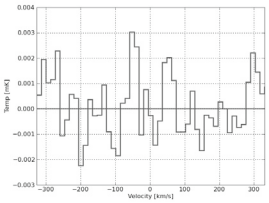

3CR 353 CO(2-1)

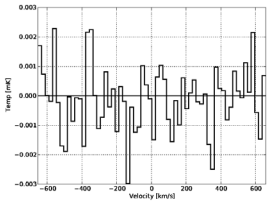

3CR 386 CO(1-0)

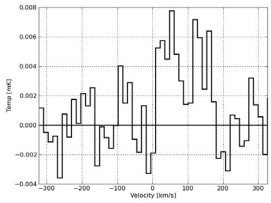

3CR 386 CO(2-1)

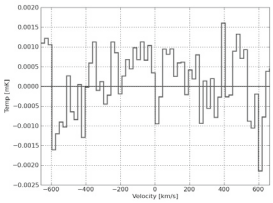

3CR 402 CO(1-0)

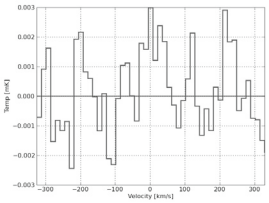

3CR 402 CO(2-1)

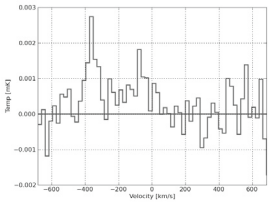

3CR 403 CO(1-0)

NO DATA AVAILABLE

3CR 403 CO(2-1)

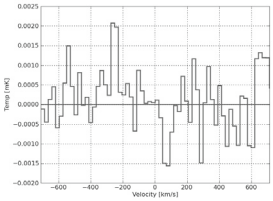

3CR 433 CO(1-0)

NO DATA AVAILABLE

3CR 433 CO(2-1)

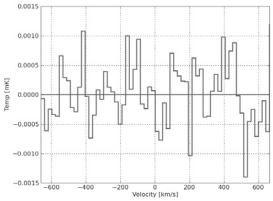

3CR 442 CO(1-0)

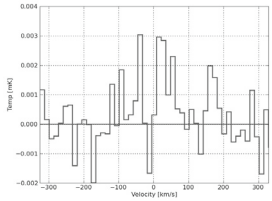

3CR 442 CO(2-1)

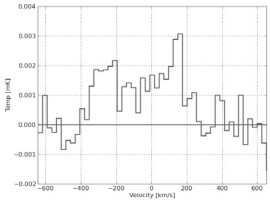

3CR 449 CO(1-0)

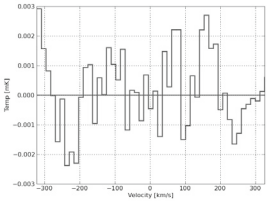

3CR 449 CO(2-1)

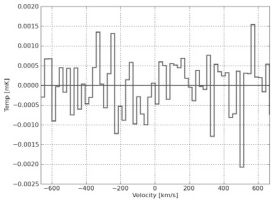

3CR 465 CO(1-0)

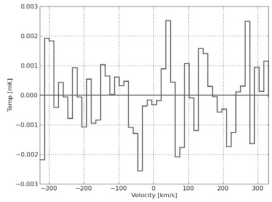

3CR 465 CO(2-1)

**Fig. 15.** continued.

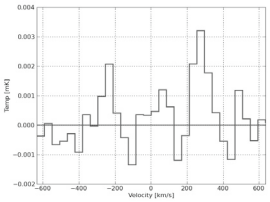
NGC 315 CO(1-0)

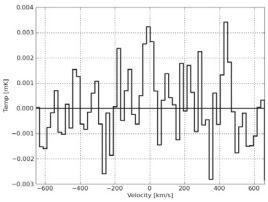
NGC 315 CO(2-1)

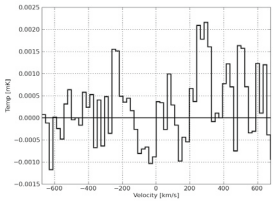
NGC 326 CO(1-0)

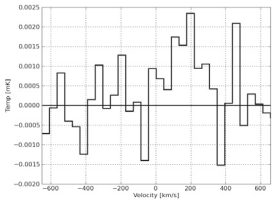
NGC 326 CO(2-1)

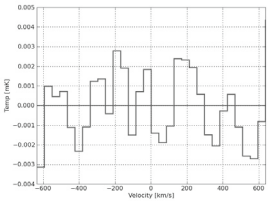
NGC 541 CO(1-0)

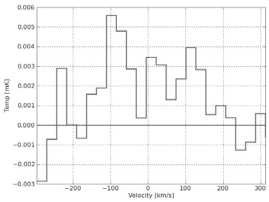
NGC 541 CO(2-1)

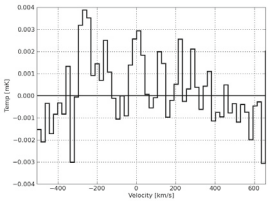
NGC 708 CO(1-0)

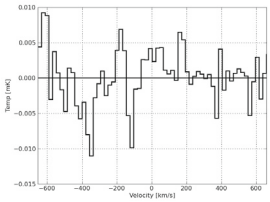
NGC 708 CO(2-1)

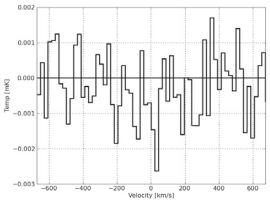
NGC 2484 CO(1-0)

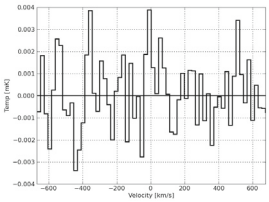
NGC 2484 CO(2-1)

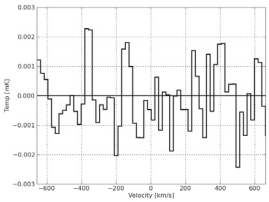
NGC 2892 CO(1-0)

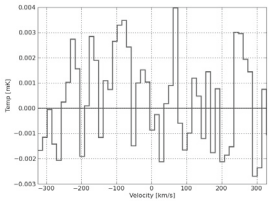
NGC 2892 CO(2-1)

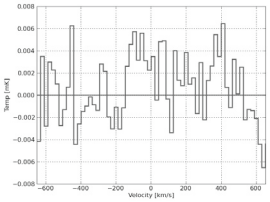
NGC 3801 CO(1-0)

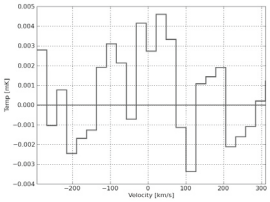
NGC 3801 CO(2-1)

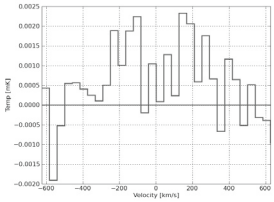
NGC 4278 CO(1-0)

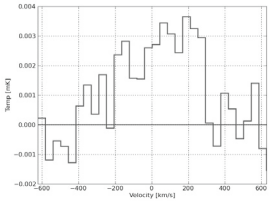
NGC 4278 CO(2-1)

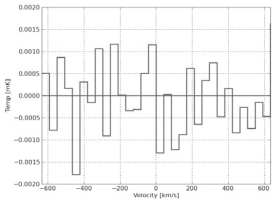
NGC 5127 CO(1-0)

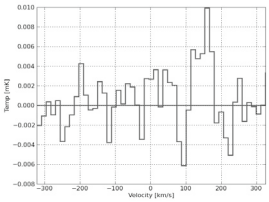
NGC 5127 CO(2-1)

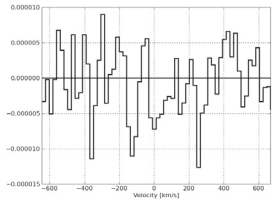
NGC 5141 CO(1-0)

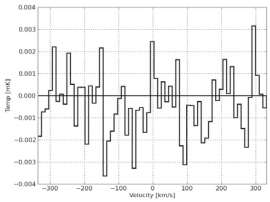
NGC 5141 CO(2-1)

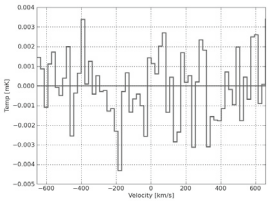
NGC 5490 CO(1-0)

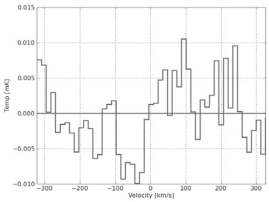
NGC 5490 CO(2-1)

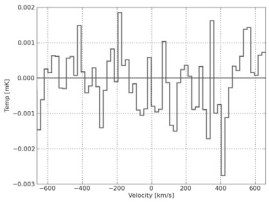
NGC 6251 CO(1-0)

NO DATA AVAILABLE

NGC 6251 CO(2-1)

**Fig. 15.** continued.

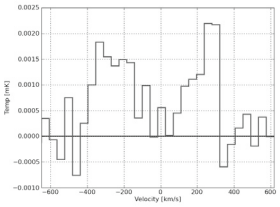
NGC 7052 CO(1-0)

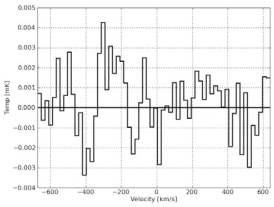
NGC 7052 CO(2-1)

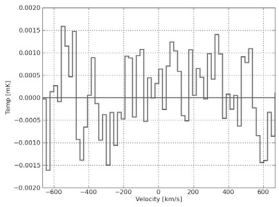
B2 0034+25 CO(1-0)

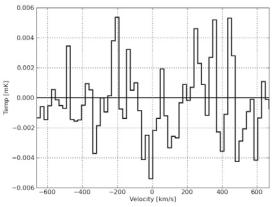
B2 0034+25 CO(2-1)

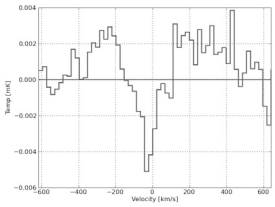
B2 0116+31 CO(1-0)

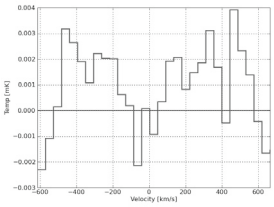
B2 0116+31 CO(2-1)

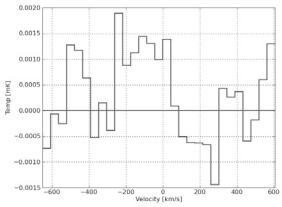
B2 0648+27 CO(1-0)

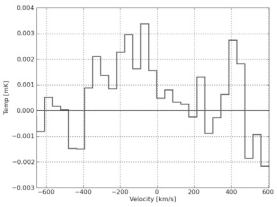
B2 0648+27 CO(2-1)

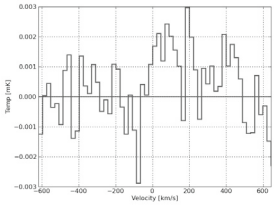
B2 0836+29B CO(1-0)

NO DATA AVAILABLE

B2 0836+29B CO(2-1)

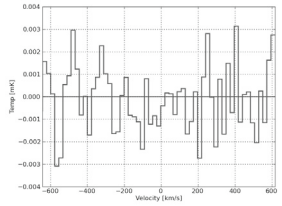
B2 0915+32B CO(1-0)

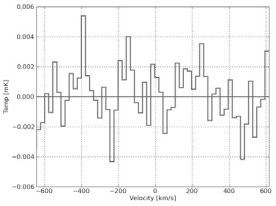
B2 0915+32B CO(2-1)

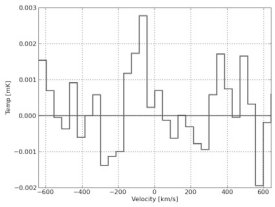
B2 0924+30 CO(1-0)

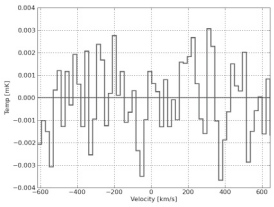
B2 0924+30 CO(2-1)

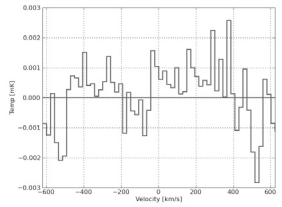
B2 1101+38 CO(1-0)

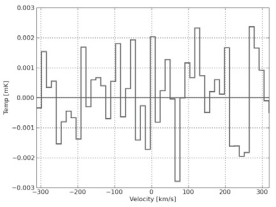
B2 1101+38 CO(2-1)

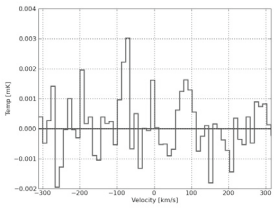
B2 1347+28 CO(1-0)

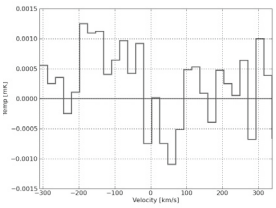
B2 1347+28 CO(2-1)

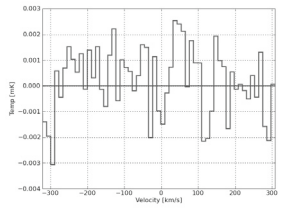
B2 1357+28 CO(1-0)

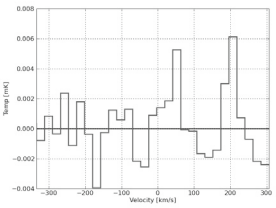
B2 1357+28 CO(2-1)

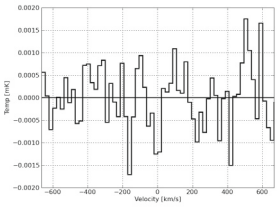
B2 1447+27 CO(1-0)

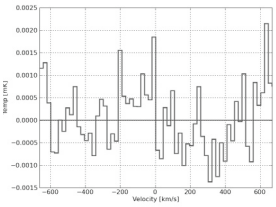
B2 1447+27 CO(2-1)

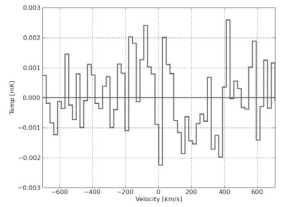
B2 1512+30 CO(1-0)

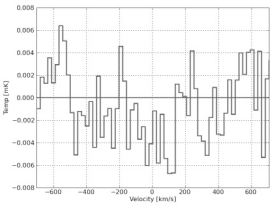
B2 1512+30 CO(2-1)

**Fig. 15.** continued.

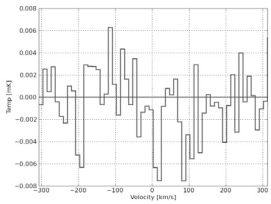

B2 1525+29 CO(1-0)

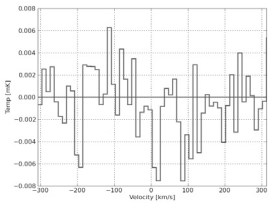

B2 1525+29 CO(2-1)

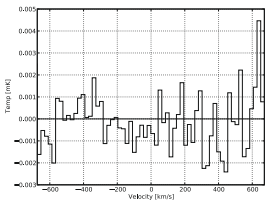

B2 1553+24 CO(1-0)

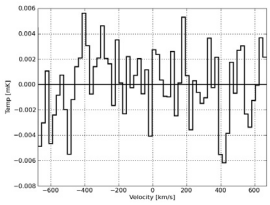

B2 1553+24 CO(2-1)

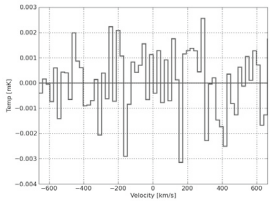

UGC 7115 CO(1-0)

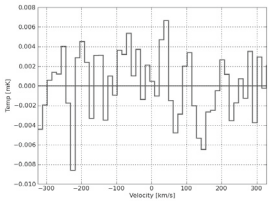

UGC 7115 CO(2-1)

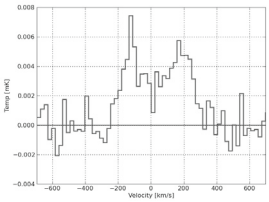

OQ 208 CO(1-0)

NO DATA AVAILABLE

OQ 208 (2-1)

**Fig. 15.** continued.